Leveraging 3D Bioprinting and Photon-Counting Computed Tomography to Enable Noninvasive Quantitative Tracking of Multifunctional Tissue Engineered Constructs

Carmen J. Gil, Connor J. Evans, Lan Li, Alex J. Allphin, Martin L. Tomov, Linqi Jin, Merlyn Vargas, Boeun Hwang, Jing Wang, Victor Putaturo, Gabriella Kabboul, Anjum S. Alam, Roshni K. Nandwani, Yuxiao Wu, Asif Sushmit, Travis Fulton, Ming Shen, Jarred M. Kaiser, Liqun Ning, Remi Veneziano, Nick Willet, Ge Wang, Hicham Drissi, Eric R. Weeks, Holly D. Bauser-Heaton, Cristian T. Badea, Ryan K. Roeder, and Vahid Serpooshan*

3D bioprinting is revolutionizing the fields of personalized and precision medicine by enabling the manufacturing of bioartificial implants that recapitulate the structural and functional characteristics of native tissues. However, the lack of quantitative and noninvasive techniques to longitudinally track the function of implants has hampered clinical applications of bioprinted scaffolds. In this study, multimaterial 3D bioprinting, engineered nanoparticles (NPs), and spectral photon-counting computed tomography (PCCT) technologies are integrated for the aim of developing a new precision medicine approach to custom-engineer scaffolds with traceability. Multiple CT-visible hydrogel-based bioinks, containing distinct molecular (iodine and gadolinium) and NP (iodine-loaded liposome, gold, methacrylated gold (AuMA), and Gd_2O_3) contrast agents, are used to bioprint scaffolds with varying geometries at adequate fidelity levels. In vitro release studies, together with printing fidelity, mechanical, and biocompatibility tests identified AuMA and Gd_2O_3 NPs as optimal reagents to track bioprinted constructs. Spectral PCCT imaging of scaffolds in vitro and subcutaneous implants in mice enabled noninvasive material discrimination and contrast agent quantification. Together, these results establish a novel theranostic platform with high precision, tunability, throughput, and reproducibility and open new prospects for a broad range of applications in the field of precision and personalized regenerative medicine.

1. Introduction

Tissue engineering scaffolds are established as robust research enabling platforms for a myriad of biomedical applications, including in vitro drug screening and disease modeling, as well as in vivo therapeutic and regenerative medicine applications. Scaffold structures, composed of 3D networks of natural and/or synthetic hydrogel biomaterials,[1–3] cells,[4,5] and small molecules,[6,7] provide a tunable microenvironment that can closely recapitulate the physiological or pathophysiological structure and/or function of native tissues and organs. However, effective application of tissue engineering products, both in vitro and in vivo, have been limited due to the lack of precise tools to non-invasively and quantitatively monitor various functions of these 3D structures.[8–11] Therefore, there is growing interest and dire need for the development of new generations of engineered scaffolds, along with advanced imaging techniques, that enable longitudinal real-time examination of scaffold function.[11–14] These functions may include the 3D construct

C. J. Gil, M. L. Tomov, L. Jin, B. Hwang, V. Putaturo, G. Kabboul, L. Ning, N. Willet, H. D. Bauser-Heaton, V. Serpooshan
Wallace H. Coulter Department of Biomedical Engineering
Emory University School of Medicine and Georgia Institute of Technology
Atlanta, GA 30322, USA
E-mail: vahid.serpooshan@emory.edu

C. J. Evans, L. Li, R. K. Roeder
Department of Aerospace and Mechanical Engineering
Bioengineering Graduate Program
Materials Science and Engineering Graduate Program
University of Notre Dame
Notre Dame, IN 46556, USA

A. J. Allphin, C. T. Badea
Quantitative Imaging and Analysis Lab
Department of Radiology
Duke University
Durham, NC 27710, USA

degradation, position, biocompatibility, blood (or culture media) perfusion and angiogenesis, and cellular functions (e.g., cell migration, fusion, proliferation, and contractile function).[14–17]

A range of non-invasive imaging modalities have been considered to monitor the performance of tissue engineering scaffolds. Magnetic resonance imaging (MRI) has been widely used to image scaffold constructs in vitro and in vivo due to exhibiting deep tissue penetration, soft tissue contrast, and high sensitivity;[8,18,19] MRI methods, however, require long acquisition times.[20] Other techniques, such as positron emission tomography (PET) and single positron emission computed tomography (SPECT), have been employed for in vivo molecular imaging of implanted scaffold structures.[21] Both PET and SPECT, however, suffer from low spatial resolution and long acquisition times and cannot provide the structural information of scaffolds.[20] Other imaging

M. Vargas, R. Veneziano
Department of Bioengineering
George Mason University
Manassas, VA 22030, USA

J. Wang, E. R. Weeks
Department of Physics
Emory University
Atlanta, GA 30322, USA

A. S. Alam
Department of Chemical and Biomolecular Engineering
Georgia Institute of Technology
Atlanta, GA 30332, USA

R. K. Nandwani, Y. Wu
Department of Quantitative Theory and Methods
Emory University College of Arts and Sciences
Atlanta, GA 30322, USA

Y. Wu
School of Civil and Environmental Engineering
Georgia Institute of Technology
Atlanta, GA 30332, USA

A. Sushmit, G. Wang
Biomedical Imaging Center
Rensselaer Polytechnic Institute
Troy, NY 12180, USA

T. Fulton, J. M. Kaiser, N. Willet, H. Drissi
Research Service
VA Medical Center
Decatur, GA 30033, USA

T. Fulton, J. M. Kaiser, N. Willet, H. Drissi
Department of Orthopedics
Emory University
Atlanta, GA 30322, USA

M. Shen, H. D. Bauser-Heaton, V. Serpooshan
Department of Pediatrics
Emory University School of Medicine
Atlanta, GA 30322, USA

L. Ning
Department of Mechanical Engineering
Cleveland State University
Cleveland, OH 44115, USA

H. Drissi
Atlanta Veterans Affairs Medical Center
Decatur, GA 30033, USA

H. D. Bauser-Heaton, V. Serpooshan
Children's Healthcare of Atlanta
Atlanta, GA 30322, USA

H. D. Bauser-Heaton
Sibley Heart Center at Children's Healthcare of Atlanta
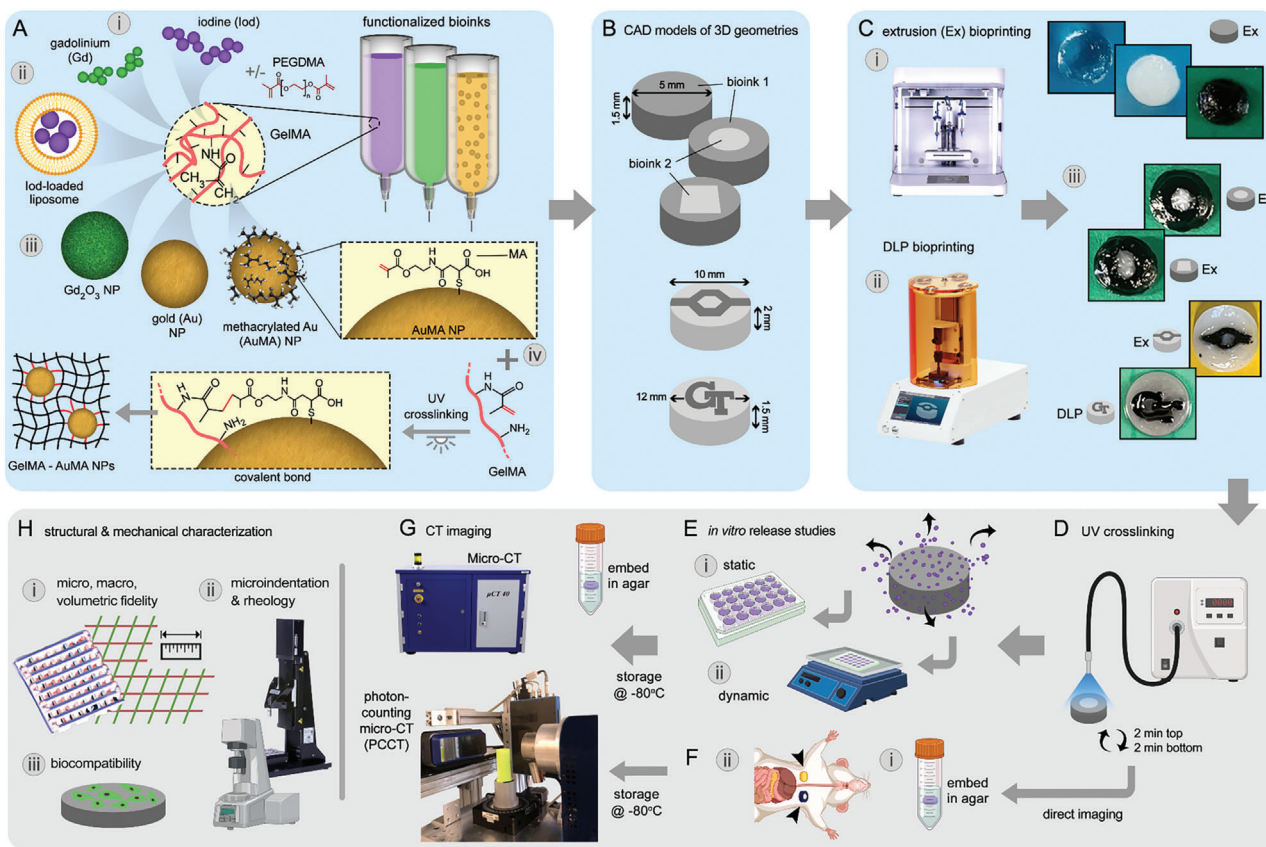Atlanta, GA 30322, USA

techniques, like optical imaging and photoacoustic microscopy, are also limited with regards to tissue penetration.[20,22]

X-ray computed tomography (CT) is a low-cost 3D imaging technique which offers high spatial resolution and deep tissue imaging[23,24] making it an attractive technology to monitor hydrogel scaffolds.[24,25] To enhance the X-ray contrast between soft tissues and hydrogels, scaffolds can be loaded with a contrast agent,[8,26] including molecular agents like gadolinium (Gd)[11] and iodine (Iod),[27] and nanomaterial agents like gold nanoparticles (Au NPs).[28] Conventional CT systems with energy integrating detectors can only discriminate a single contrast agent, due to an inability to differentiate between multiple materials exhibiting similar overall X-ray attenuation across the photon energy spectrum. However, photon-counting CT (PCCT) acquires images in multiple photon energy bins that can be selected to leverage characteristic differences in the X-ray attenuation of different materials across the incident photon energy spectrum and subsequently decomposed into multiple material-specific images.[29,30] Thus, spectral (or multicolor) PCCT can accurately identify and quantify multiple materials, including contrast agents and tissues, simultaneously.[31–33] Non-destructive spectral PCCT further offers a unique possibility to distinguish multiple scaffold functions and biological processes.[34,35]

The incorporation of multiple distinct imaging contrast agents within 3D scaffolds requires advanced biomanufacturing techniques to control their spatial distribution within the 3D matrix. 3D bioprinting allows precise control of bioink composition, properties, and printing parameters for fabricating highly complex and heterogenous scaffolding systems as novel personalized and precision medicine therapies for a wide variety of tissues and organs.[36–41] Bioprinted implants have demonstrated accelerated tissue repair, increased angiogenesis, reduced scar size, and improved function in various animal models, including cardiac,[42–44] osteochondral,[45,46] neural tissue,[47,48] and skin[49,50] injury models. There has been, however, no systematic study to examine the combined use of 3D bioprinting and multi-contrast CT imaging for creating and monitoring multimaterial scaffolding systems. This study investigates the feasibility of incorporating multiple CT contrast agents in 3D bioprinted constructs, and the use of PCCT to visualize these complex geometries. In-depth analysis and optimization of printing fidelity, retention/release of contrast agents, and mechanical properties were performed for bioinks loaded with a variety of CT contrast agents, including both molecular (Iod and Gd) and NP (Iod-loaded NP, Au, methacrylated Au (AuMA) and Gd_2O_3) contrast agents.

2. Results and Discussion

The unique capability of 3D bioprinting platforms in offering precise spatiotemporal control of biological reagents within the 3D space, provides the opportunity to create heterogenous tissue structures, laden with a variety of imaging contrast agents.[51] In this study, we leveraged multi-material 3D bioprinting and PCCT technologies to establish a precision medicine platform for non-invasive, longitudinal, and 3D monitoring of tissue engineered scaffolds both in vitro and ex vivo (postmortem mouse model) (**Figure 1**).

Figure 1. Schematic illustration of the research workflow in this study. A) Various computed tomography (CT) contrast agents were incorporated in gelatin methacrylate (GelMA), with and without polyethylene glycol dimethacrylate (PEGDMA), to create functionalized bioinks. These included molecular iodine (Iod) and gadolinium (Gd) contrast agents (i), Iod-loaded liposome nanocapsule (ii), and nanoparticle (NP) contrast agents, namely Gd_2O_3, gold (Au), and methacrylated gold (AuMA) NPs (iii). A one-step UV-photopolymerization of GelMA and AuMA NPs was used to form covalent linkages and prepare GelMA-Au NP hydrogels (iv). Adapted with permission under the terms of the CC-BY license.[53] Copyright 2022, the Authors. Published by Wiley-VCH GmbH. B) CAD models of scaffolds with varying geometries were created and assigned to distinct CT contrast agent-laden bioinks. C) 3D bioprinting of CT-visible bioink formulations was conducted using either extrusion (Ex) (i) or digital light processing (DLP)-based (ii) techniques to create 3D constructs of varying geometry (iii). D) Printed constructs were crosslinked immediately post print under varying UV intensity for a 4-min duration (2×2 min, flipping the construct at midpoint). E) A group of extrusion-printed constructs (simple disc geometry) were used to study contrast agent release under static (i) versus dynamic (ii) conditions in PBS. At each time point, constructs were retrieved from the solution, embedded in agar, and stored at −80 °C (to avoid further release) until micro-CT imaging. F) A separate group of printed constructs consisting of multiple distinct contrast agents in varying geometries were immediately embedded in agar, stored at −80 °C, and imaged via micro-CT and photon-counting CT (PCCT) either in vitro (in agar) (i) or after subcutaneous implantation in the mouse torso (ii). G) CT imaging of various experimental groups were performed either via micro-CT (i) (for release study) or spectral PCCT (ii). H) Structural, mechanical, and biological characterization of bioinks and printed constructs were performed using micro, macro, and volumetric fidelity analyses (i), microindentation and rheological analyses (ii), and cell viability and growth assays (iii).

To identify and prepare optimal CT-visible bioink compositions, several molecular (Gd, Iod) and NP-based contrast agents (Iod-loaded liposome, Au, AuMA, and Gd2O3) were selected and incorporated into various GelMA-based hydrogel bioinks (Figure 1A). For the digital light processing (DLP)-based bioprinting, polyethylene glycol dimethacrylate (PEGDMA) was added to the GelMA, to provide adequate mechanical properties, porosity, and overall stability of printed hydrogel constructs.[52] For Au NP contrast agents, while increase in NP concentration could yield greater X-ray attenuation and CT contrast,[26,53] it could also significantly disturb the photocrosslinking of bioprints due to the absorption and scattering of UV and visible light.[54] To address this issue, two sets of GelMA-based bioinks were formulated via physical mixing of the Au NPs in 20% GelMA (20.2 mM NPs),

or by using previously reported AuMA NPs[53] (10 mM NPs) that participated in photocrosslinking to form covalent linkages with GelMA molecules (Figure 1A-iii,iv). Various scaffold geometries were designed and fabricated using extrusion or DLP-based bioprinting modalities (Figure 1B,C). The stability of incorporated contrast agents in the printed constructs was carefully examined via quantitative in vitro release analyses (Figure 1D,E). Bioprinted constructs, consisting of single or double contrast agents, were imaged using micro-CT and spectral PCCT systems (Figure 1G). In-depth fidelity and mechanical testing were also performed on the bioinks and bioprints to assess and optimize printability and stability of the developed scaffolding systems (Figure 1H).

In this study, 12% GelMA concentration was used as the optimal bioink formulation, as established in our prior works.[12,55,56]

**ADVANCED
SCIENCE NEWS**

www.advancedsciencenews.com

**ADVANCED
HEALTHCARE
MATERIALS**

www.advhealthmat.de

The 20% GelMA solution was used specifically for the Au and AuMA NP ink groups, where the 12% GelMA concentration was not sufficient to maintain adequate printability and crosslinking of constructs. The concentration of each contrast agent in GelMA was selected as the lowest value that would generate clinically relevant X-ray attenuation (200–300 HU[57]). The 20% GelMA solution and LAP photoinitiator was used specifically for the Au and AuMA NP ink groups, following previously established methods to optimize the photocrosslinking of constructs containing sufficient Au concentrations for X-ray contrast.[53] Due to the interference of NPs with photocrosslinking process, a rather long UV irradiation time was used for the 12% GelMA groups with Irgacure photoinitiator (4 min, 7 mW cm^{-2}), while 20% GelMA bioinks used the LAP photoinitiator and the safe blue light crosslinking (4 min, 30 mW cm^{-2}). The potential adverse effects of such UV exposure[58] when printing with cells should be taken into consideration in future studies.

A key aspect to be considered when designing and developing new bioink formulations is the bioprintability and printing fidelity of the hydrogel materials.[53,55,59] This is particularly important for NP-modified bioink solutions, where the incorporated particles could pose potential interference with the rheological properties of hydrogel inks, and hence, deteriorate their printability.[10,19,53,60] In this study, we examined the printability of bioink formulation containing various contrast agents by quantifying the microscopic (strand-level, **Figure 2**A–E) and macroscopic (bulk, Figure 2F) fidelity, as well as the rheology properties of bioinks (Figure S2, Supporting Information). Microfidelity of bioink solutions based on the 12% (Figure 2B) and 20% (Figure 2D) GelMA were analyzed separately to allow for direct comparison across groups (**Table 1**). Bioprinted (extruded) strands showed a relatively large variation in r_d (strand diameter) ratios, in reference to the CAD design, ranging from 1.1 (blank GelMA control bioinks) to 2.1 (Iod-loaded liposome NPs) (Figure 2B–E and Table 1). While the blank GelMA bioinks showed proper printability, the large deviation among other groups could be attributed to the potential role of added imaging agents to the bioinks, particularly to the NP supplements which could significantly alter the rheology and extrusion properties of the bioinks.[61,62] This could be particularly the case for the Iod-loaded liposome group which had the highest NP size as determined by dynamic light scattering (DLS) (300–400 nm) (Figure S1, Supporting Information). Other factors contributing to strand diameter deviations could include the potential swelling/shrinkage of extruded filaments, the surface tension properties of various bioinks, and/or the collapse/deformation caused by gravity, prior to crosslinking.[63] Further optimization of the printing process could be performed for each functionalized bioink through more precise tuning of printing pressure, temperature, and speed.[62] Among NP-loaded bioinks, the AuMA NP group showed the best fidelity (r_d ratio) which was significantly ($P < 0.005$) improved in comparison to Au NP-containing bioink. This could be attributed to the unique capability of AuMA NPs, as a new photopolymerizable X-ray contrast agent, to form covalent linkages to GelMA in a single step during photocrosslinking.[53] Of note, other fidelity measurements for the strand angle ratio (r_α), uniformity ratio (r_U), and interstrand area ratio (r_A) showed values close to 1.0 (ranging from 0.94 to 1.09) for all bioink groups, indicating a high level of precision in other geometrical features of printed strands (Figure 2B–E and Table 1). Overall, these results indicate adequate microscale printability of the functionalized bioink solutions developed in this study.

In addition to the microscopic fidelity, we also assessed the bulk (macro-scale) fidelity of the disc-shape constructs printed with various bioinks (Figure 2F). Measurements of the disc diameter (r_D) ratio before and after crosslinking showed consistent and reliable printing of the disc structure for all bioink groups which ranged from 0.96 to 1.05 (Table 1 and Figure 2F). In comparison to the normal Au NP bioink, the AuMA NP group showed enhanced printing fidelity (0.98 ± 0.01), consistent with the strand fidelity measurements demonstrated above (Figure 2D). Of note, crosslinking of extruded constructs did not result in a significant ($P > 0.05$) alteration in constructs' dimensions. Overall, the micro and macro fidelity results show adequate printability of bioink solutions, particularly in the bulk scales. Further improvement in the precision and reproducibility of bioprints could be explored by conducting in-depth rheology assays to determine optimal printing parameters (e.g., temperature, pressure, and speed).[56] Among NP contrast agents, Gd_2O_3 and AuMA NPs showed the best fidelity when incorporated into GelMA bioinks, which could be attributed to their relatively small size (20–80 nm for Gd_2O_3 and 12 nm for AuMA, **Table 2**), minimal interference with photocrosslinking, and the enhanced mixing of MA-ligands (in AuMA NPs) with GelMA.[53] Therefore, Gd_2O_3 and AuMA NPs were selected as main bioink groups for the in vitro and animal PCCT imaging.

The incorporation of contrast agents into the hydrogel solutions has been established as an effective method to tailor various physiomechanical properties of these scaffolding biomaterials to adapt for a variety of biomedical applications.[19,64-66] To examine the effect of incorporated molecular and NP contrast agents with different sizes on the mechanical properties of bioprints, microindentation test was performed on simple cubic constructs printed using various inks (Figure 2G). In comparison to the control 12% (blank) GelMA group, the addition of molecular agents, that is, Gd chelate and Iod both in bare form and loaded in liposome nanocapsules, resulted in significant increases in the elastic modulus of bioprints. Namely, the modulus increased from 57.7 ± 3.0 kPa in 12% GelMA, to 79.6 ± 9.8 kPa for Gd chelate ink, and 100.9 ± 8.6 kPa for Iod ink, and 142.6 ± 14.2 kPa (mean ± standard error of the mean (SEM)) for Iod-loaded liposome group. These results are in line with previous reports indicating enhanced mechanical properties of biomaterials following inclusion of Gd and Iod reagents.[67-70] Constructs fabricated with Au NP bioink showed significantly lower elastic modulus (23.9 ± 2.0 kPa) compared to the 20% GelMA control (142.2 ± 17.1 kPa). This may be due to disrupting effect of Au NPs on the GelMA hydrogel network by their physical size upon entrapment and/or their absorption/scattering of UV light during photocrosslinking.[53,54,71] Importantly, AuMA NP bioprints yielded significantly higher ($P < 0.005$) modulus compared to the Au NP group and were not significantly different from the blank GelMA control (109.5 ± 5.8 kPa) (Figure 2G). The enhanced mechanical properties of AuMA NP-loaded constructs in comparison to Au NP could be attributed to the ability of AuMA NPs to participate in photocrosslinking and form covalent linkages with GelMA molecules, minimizing disruption of the hydrogel net-
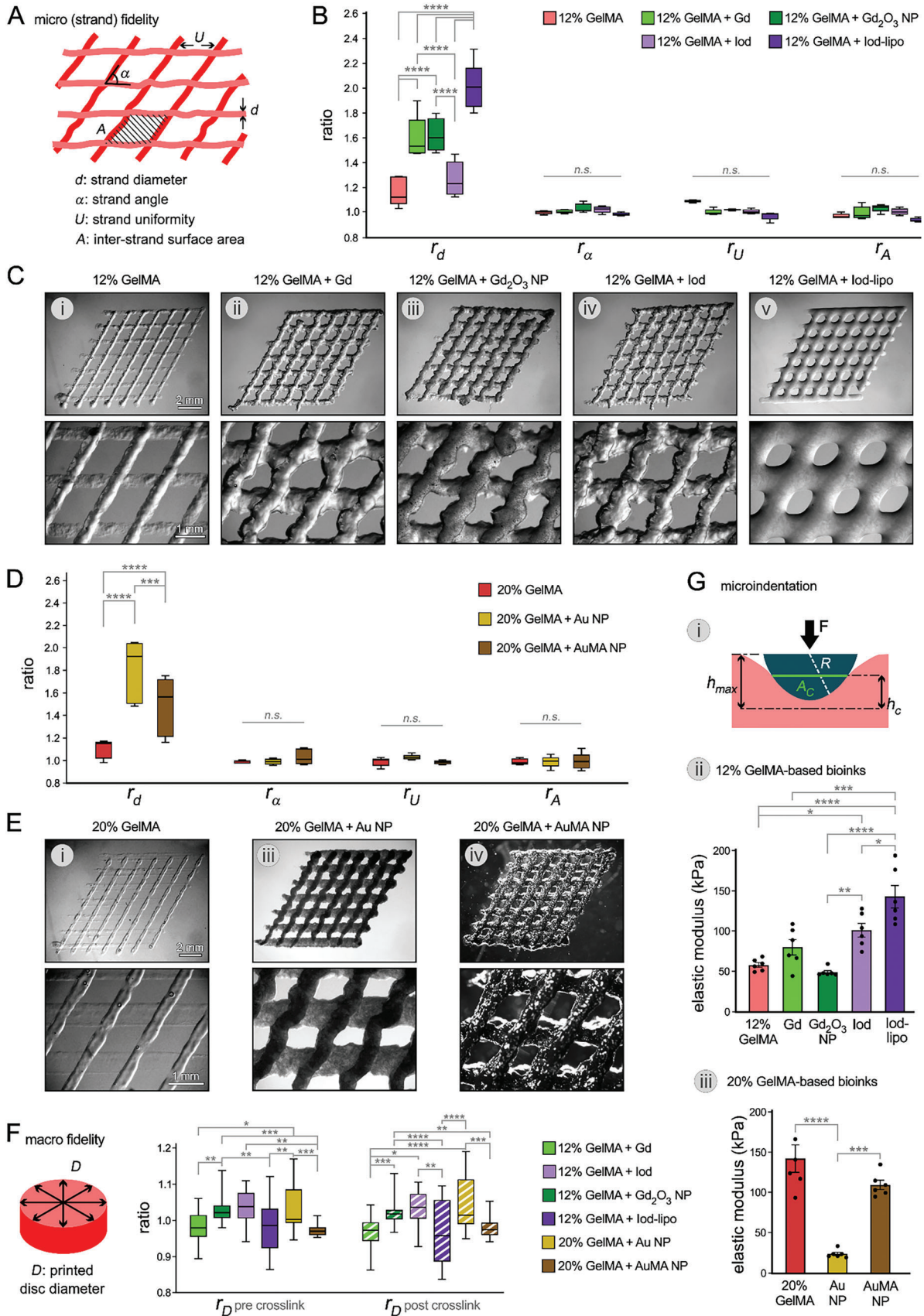
A. micro (strand) fidelity

d: strand diameter
α: strand angle
U: strand uniformity
A: inter-strand surface area

B. (box plots: r_d, r_α, r_U, r_A)

Legend: 12% GelMA; 12% GelMA + Gd; 12% GelMA + Gd$_2$O$_3$ NP; 12% GelMA + Iod; 12% GelMA + Iod-lipo

C. 12% GelMA (i); 12% GelMA + Gd (ii); 12% GelMA + Gd$_2$O$_3$ NP (iii); 12% GelMA + Iod (iv); 12% GelMA + Iod-lipo (v)

D. (box plots: r_d, r_α, r_U, r_A)

Legend: 20% GelMA; 20% GelMA + Au NP; 20% GelMA + AuMA NP

E. 20% GelMA (i); 20% GelMA + Au NP (iii); 20% GelMA + AuMA NP (iv)

F. macro fidelity

D: printed disc diameter

(r_D pre crosslink; r_D post crosslink)

Legend: 12% GelMA + Gd; 12% GelMA + Iod; 12% GelMA + Gd$_2$O$_3$ NP; 12% GelMA + Iod-lipo; 20% GelMA + Au NP; 20% GelMA + AuMA NP

G. microindentation (i)

ii. 12% GelMA-based bioinks (elastic modulus (kPa): 12% GelMA; Gd; Gd$_2$O$_3$ NP; Iod; Iod-lipo)

iii. 20% GelMA-based bioinks (elastic modulus (kPa): 20% GelMA; Au NP; AuMA NP)

Table 1. Results for the measurement of micro- and macro- fidelity of various bioinks and bioprinted constructs used in this study.

Bioink		12% GelMA	20% GelMA	Iod	Gd	Gd$_2$O$_3$ NP	Au NP	AuMA NP	Iod-liposome
Micro Fidelity	Strand diameter ratio (r_d)	1.17 ± 0.05	1.10 ± 0.04	1.27 ± 0.06	1.59 ± 0.08	1.62 ± 0.06	1.80 ± 0.13	1.80 ± 0.12	2.01 ± 0.09
	Strand angle ratio (r_α)	1.00 ± 0.01	0.99 ± 0.01	1.02 ± 0.01	1.00 ± 0.01	1.03 ± 0.02	0.99 ± 0.01	1.03 ± 0.03	0.99 ± 0.01
	Strand uniformity ratio (r_U)	1.09 ± 0.01	0.99 ± 0.05	1.00 ± 0.01	1.00 ± 0.01	1.02 ± 0.00	1.03 ± 0.01	0.98 ± 0.01	0.97 ± 0.02
	Inter-strand area ratio (r_A)	0.97 ± 0.01	0.99 ± 0.01	1.00 ± 0.01	0.99 ± 0.02	1.03 ± 0.01	0.99 ± 0.02	0.99 ± 0.03	0.94 ± 0.01
Macro fidelity	Disc diameter ratio (r_D)	1.05 ± 0.01%	1.02 ± 0.01%	1.04 ± 0.01	0.97 ± 0.01	1.02 ± 0.01	1.04 ± 0.01	0.98 ± 0.01	0.97 ± 0.02

GelMA: gelatin methacrylate. Iod: iodine. Gd: gadolinium. Au: gold. NP: nanoparticle. AuMA: methacrylated gold.

Table 2. Summary of the bioink groups synthesized and used in this study.

Bioink	GelMA bioink (1)	GelMA bioink (2)	Iod bioink	Gd bioink	Gd$_2$O$_3$ bioink	Au Bioink	AuMA bioink	Iod-liposome bioink
[GelMA] wt%	12%	20%	12%	12%	12%	20%	20%	12%
PI type, [PI] w/v%	Irgacure, 0.6%	LAP, 0.5%	Irgacure, 0.6%	Irgacure, 0.6%	Irgacure, 0.6%	LAP, 0.5%	LAP, 0.5%	Irgacure, 0.6%
Contrast agent type	—	—	Molecular	Molecular	NP	NP	NP	NP
Contrast agent features	—	—	Omnipaque 350	Gadavist	Gd$_2$O$_3$ NP 20–80 nm	Aurovist 15 nm	AuMA NP 12 nm	Iod-loaded liposome NP 300–400 nm
[Contrast agent] [mM]	—	—	49.8	41.5	22.3	20.2	10.0	49.8

NP: nanoparticle. GelMA: gelatin methacrylate. PI: photoinitiator. Iod: iodine. Gd: gadolinium. Au: gold. AuMA: methacrylated gold.

work, consistent with our previous report.[53] The enhancement of mechanical properties of scaffolds, in addition to generating imaging contrast, could further expand the applications of tissue engineered constructs in diverse clinical applications. Such mechanisms could be particularly of great significance in hard (e.g., bone) tissue regenerative therapies, where the elastic modulus of hydrogel scaffolds needs major enhancement to match the native tissue stiffness.[72,73]

We also examined the rheological properties and stability of bioink solutions over time by conducting time sweep assays (Figure S2, Supporting Information). Both 12 and 20% GelMA hydrogels (without NPs) showed time-independence in their storage modulus, G', and loss modulus, G'', consistent with previous reports.[56] For GelMA bioinks containing AuMA and Gd$_2$O$_3$ NPs, however, G' increased over time, indicating an increase in stiffness (Figure S2A, Supporting Information). The increase in G' might be explained by NP aggregation[74,75] and/or thermally induced photocrosslinking.[76] We also performed temperature sweep experiments from 15 to 40 °C, which encompasses all printing temperatures (Figure S2B, Supporting Information).

The gelling temperature was determined by the crossover of G' and G'' at 23 °C for 12% GelMA, 26 °C for 20% GelMA, 32 °C for 12% GelMA + Gd$_2$O$_3$ NP, and 26 °C for 20% GelMA + AuMA NP.

Following printing fidelity and biomechanical characterization of novel bioink formulations, we evaluated the stability of bioprinted constructs with regards to the retention of incorporated contrast agents which would be of great significance for both in vitro and in vivo imaging of these scaffolding systems.[8-10] Further, longitudinal and quantitative examination of the release profile of incorporated reagents at various molecular sizes would provide a robust method to evaluate and predict the release profile for a variety of therapeutic reagents at comparable sizes. Therefore, the feasibility of novel bioinks as a platform for longitudinal noninvasive monitoring of bioprinted constructs was verified by measuring the X-ray attenuation of constructs printed with different bioinks at contrast agent concentrations that generate clinically relevant CT signal (**Figure 3**). Standard (calibration) curves were first generated for the molecular (Gd chelate and Iod, Figure 3A) and NP (Figure 3F) contrast agents. Accord-

Figure 2. Characterization of printing fidelity and mechanical properties of bioprinted CT-visible GelMA constructs. A) The design of a two-layer model used to assess 2D micro-scale (strand-level) fidelity. B) Quantification of micro-scale fidelity parameters for various bioinks, including the strand diameter ratio (r_d), angle ratio (r_α), uniformity ratio (r_U), and inter-strand area ratio (r_A) ($n = 5$ per group). The 12% GelMA-based bioink groups included the bare GelMA (control), GelMA containing gadolinium (Gd) and iodine (Iod) molecular contrast agents, and GelMA containing Gd$_2$O$_3$ and Iod-loaded liposome nanoparticles (NPs). C) Qualitative evaluation of printed strands consisting of various bioinks via bright-field imaging of strands at two magnifications. D,E) Quantitative (D) and qualitative (bright field images) (E) analysis of strand fidelity, conducted for various 20% GelMA-based bioink formulations ($n = 5$ per group), including pure GelMA (control), and those loaded with gold (Au) and methacrylated gold (AuMA) NPs. F) Macro-scale fidelity analysis was conducted for all bioink groups by measuring the diameter of a disc-shape construct and comparing with the CAD values (disc diameter ratio, r_D) ($n = 4$ per group). G) Microindentation test (**i**) was conducted on 12% (ii) and 20% (iii) GelMA-based bioink formulations to quantify the elastic modulus (E) ($n = 6$ per group). Scale bars in top rows in (C) and (E) represent 2 mm and in bottom rows represent 1 mm. *$P < 0.05$, ***$P < 0.005$, and ****$P < 0.001$. n.s.: not significant.
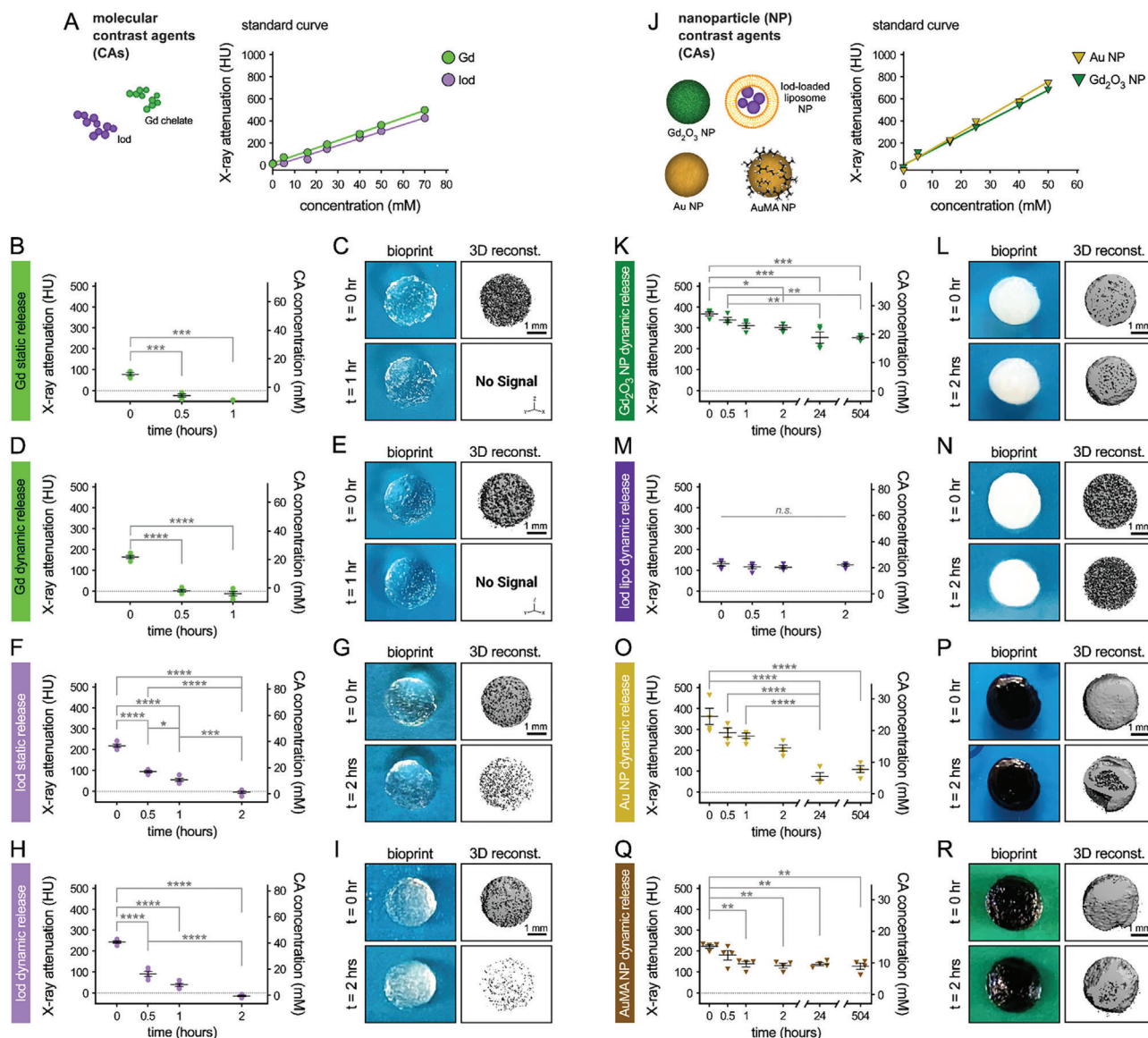
Figure 3. In vitro characterization of the retention of various molecular and nanoparticle (NP) contrast agents from 3D bioprinted GelMA constructs. A) Standard curves of Gd chelate and Iod (molecular) contrast agents. B–E) In vitro release of Gd chelate from bioprints under (B) and (C) static and (D) and (E) dynamic (rocking) conditions in PBS for a 1-h duration ($n = 4$ per group). C,E) Corresponding micro-CT reconstructions at $t = 0$ and 1 h post-incubation. "No signal" labels indicate that no detectable CT signal was obtained at indicated time points. F–I) In vitro release of Iod from bioprints under F,G) static and H,I) dynamic conditions in PBS for a 2-h duration ($n = 4$ per group). G,I) Corresponding micro-CT reconstructions at $t = 0$ and 2 h post incubation. J) Standard curves of Gd_2O_3 and Au NP contrast agents. K,L) In vitro release of Gd_2O_3 NPs from bioprints under dynamic conditions in PBS for a 504-h (3-week) duration ($n = 4$ per group) (K), and corresponding micro-CT reconstructions at $t = 0$ and 2 h (L). M,N) In vitro release of Iod from Iod-loaded liposome nanocapsules in the bioprints under dynamic conditions in PBS for a 2-h duration ($n = 4$ per group) (M) and the corresponding micro-CT reconstructions (N) at $t = 0$ and 2 h. O,P) In vitro release of Au NPs from bioprints under dynamic conditions in PBS for a 504-h (3-week) duration ($n = 4$ per group) (O) and the corresponding micro-CT reconstructions (P) at $t = 0$ and 2 h. Q,R) In vitro release of AuMA NPs from bioprints under dynamic conditions in PBS for a 504-h (3-week) duration ($n = 4$ per group) (Q) with the corresponding micro-CT reconstructions (R) at $t = 0$ and 2 h. All scale bars represent 1 mm. $*P < 0.05$, $**P < 0.01$, $***P < 0.005$, and $****P < 0.001$.

ing to the obtained standard curves, the lowest concentration of contrast agent to achieve an X-ray attenuation readily detected with preclinical scanners (200–300 HU[57]) was chosen to investigate retention. Longitudinal studies for the molecular contrast agents demonstrated a quick (burst) release of reagents within a 1-h (Gd) or 2-h (Iod) window in static and dynamic (rocking) conditions (Figure 3B–I). The Gd release studies were stopped

after 1 h as there was no detectable CT signal at $t > 1$ h. The burst release was most likely due to the small molecular size of Gd chelate and Iod (500–850 Da, <1 nm[77]) in comparison to the GelMA pore size (≈5–50 μm[78,79]), permitting rapid depletion (diffusion) of the reagents. Samples images at $t = 2$ h confirmed an intact scaffold structure, suggesting that diffusion was the primary release mechanism for Gd and Iod.[80,81] Further, 3D

**ADVANCED
SCIENCE NEWS**

www.advancedsciencenews.com

**ADVANCED
HEALTHCARE
MATERIALS**

www.advhealthmat.de

micro-CT reconstructions at $t = 2$ h confirmed that there was little to no contrast agent remaining in the constructs. Incorporation of such imaging probes in bioprinted constructs would be, therefore, not appropriate for imaging applications (particularly in vivo) and would not offer CT visibility over prolonged time periods.

We subsequently tested the stability/retention of bioinks loaded with various NP contrast agents, which in most cases demonstrated adequate retention in the constructs (Figure 3J–R). Considering the greater stability from NP-loaded constructs, we only conducted the more aggressive release assays under dynamic conditions for these groups. Gd_2O_3 NP-loaded bioprints exhibited a slow release at early time points (0–24 h), which then reached a plateau for >24 h (Figure 3K–L). Iod-loaded liposome NPs were not released from constructs over 2 h ($P > 0.05$) (Figure 3M,N). For both Gd_2O_3 NP and Iod-liposome groups, samples photos and micro-CT reconstructions confirmed small release and rather intact signal after dynamic incubation in phosphate buffer saline (PBS) (Figure 3L,N and Figure S3A, Supporting Information). In contrast, the Au NP bioprints showed a significant release and depletion from constructs, particularly over the first 24 h, which then reached a plateau for $t = 24$ to 504 h (Figure 3O,P). Of note, while the samples photos showed rather intact scaffold structures, the micro-CT reconstructions revealed noticeable depletion of Au NPs from the constructs, particularly from the central areas of the bioprints (Figure 3P, Figure S3B, Supporting Information). After 504 h (3 weeks) of incubation, Au NPs were entirely depleted from the central area of the construct (Figure S3B, Supporting Information). These results suggest diffusion-mediated release of these NPs. The nonuniform release of Au NPs was most likely caused by the incomplete GelMA photocrosslinking due to significant absorption of UV light by Au NPs,[54,82] which could deteriorate the structural integrity, particularly in the center of the construct with the lowest amount of crosslinking.[53] To resolve the poor retention and disrupted photocrosslinking with Au NPs, we methacrylated Au NPs that were subsequently able to be mixed with GelMA the same way as other bioink formulations; however, unlike other NP contrast agents that were physically mixed with GelMA, AuMA NPs were covalently linked to the GelMA polymer chain during photocrosslinking.[53]

In contrast to the Au NP behavior, AuMA NPs exhibited a relatively stable retention within the bioprints, with a slight decrease in signal at the first hour, followed by a plateau for the remaining 3-week incubation in PBS (Figure 3Q,R). Samples photos and micro-CT reconstructions confirmed only a slight release of AuMA NPs (Figure 3R, Figure S3C, Supporting Information). Reduced pore size as a result of increasing GelMA concentration, from 12% to 20% (as reported before[83,84]), could have contributed significantly to the enhanced NP retention within the constructs. Although, the reduced pore size would not likely affect the retention of Gd and Iod small molecules (<1 nm[77]), which were not comparable in size with the NPs (10–400 nm). SEM analysis of DLP bioprinted GelMA constructs in this study demonstrated a highly porous structure with mean pore size of 95.3 ± 34.4 µm (Figure S4, Supporting Information) which was consistent with prior reports.[83] Overall, the bioprinted constructs loaded with Gd_2O_3 and AuMA NP contrast agents demonstrated adequate retention and showed promise for the long-term, quantitative, and longitudinal tracking of bioprinted tissue engineered products in the in vitro and in vivo applications.

The biocompatibility of GelMA-based hydrogels and NP systems used in this study have been already extensively evaluated and confirmed in prior works.[19,53,56,85,86] To further assess biocompatibility of GelMA bioinks loaded with Gd_2O_3 and AuMA NPs, we performed 7-day culture of HUVECs onto each substrate and examined cell viability and growth via Live/Dead and AlamarBlue assays (Figure S5, Supporting Information). Results demonstrated significant cell viability and proliferation over the culture period (10–20% AlamarBlue reduction % after 7 days of culture), achieving almost confluent monolayers in all bioink groups. More in-depth bioactivity assays would be required in the future to assess the functionality of specific types of cells, for specific tissue engineering applications, while cells cultured on 2D and/or encapsulated in 3D bioink constructs.

Spectral PCCT is an emerging imaging modality which may enable non-invasive, quantitative detection and monitoring of 3D bioprinted constructs for both in vitro and (more importantly) in vivo applications. To evaluate this concept, constructs of different spatial designs containing AuMA and Gd_2O_3 NP contrast agents were bioprinted and imaged using conventional micro-CT and spectral PCCT (**Figure 4**). Concentric circle (ConC), rectangle in circle (RinC), vascular tree in circle (VasC), and the Georgia Tech logo (GT) designs were created via CAD (Figure 4A–D-i) and bioprinted at high spatial fidelity (Figure 4A–D-ii). To examine the feasibility of various printing modalities, ConC and RinC models were created using micro-extrusion bioprinting and the GT logo was prepared using DLP-based bioprinting. For both printing modalities, multi-material (contrast) geometries were reliably and reproducibly fabricated ($n > 8$). Visibly white regions in the printed designs comprised the Gd_2O_3 NP bioink, while visibly dark regions comprised the AuMA NP bioink.

Axial slices from conventional CT images (Figure 4A–D-iii) provided a coarse view of the internal construct geometry. However, these single-energy, grayscale images lacked the ability to clearly distinguish material boundaries and quantify material concentrations. Spectral PCCT (Figure 4A–D-iv), on the other hand, provided higher contrast single-energy bin images (grayscale, top left) and provided a spatial map of Au and Gd_2O_3 concentrations. We also presented these quantitative maps as color-coded images in which the red and green intensities correspond to Au and Gd_2O_3 concentration, respectively. An axial slice (top right), coronal slice (bottom left), and 3D rendering (bottom right) are also shown to visualize the multimaterial construct (Figure 4A–D-iv). The presence of Au in the center of VasC and GT logo designs and Gd_2O_3 in the center of ConC and RinC designs demonstrated the robust quantification of contrast agents regardless of spatial position. Additionally, the 3D nature of these images allowed for material quantification despite depth-dependent printing irregularities. Overall, PCCT imaging enabled visualization of contrast agents that were measured to exhibit concentrations ranging from 2.5 to 25 mM for AuMA NPs and from 7 to 37 mM for Gd_2O_3 NPs.

To evaluate the precision and reproducibility of scaffold features in PCCT images for various scaffold geometries, we compared measurements of feature dimensions in CT images with the CAD model or the printed construct (Figure 4E,F). For the ConC design, PCCT images exhibited a larger inner diameter
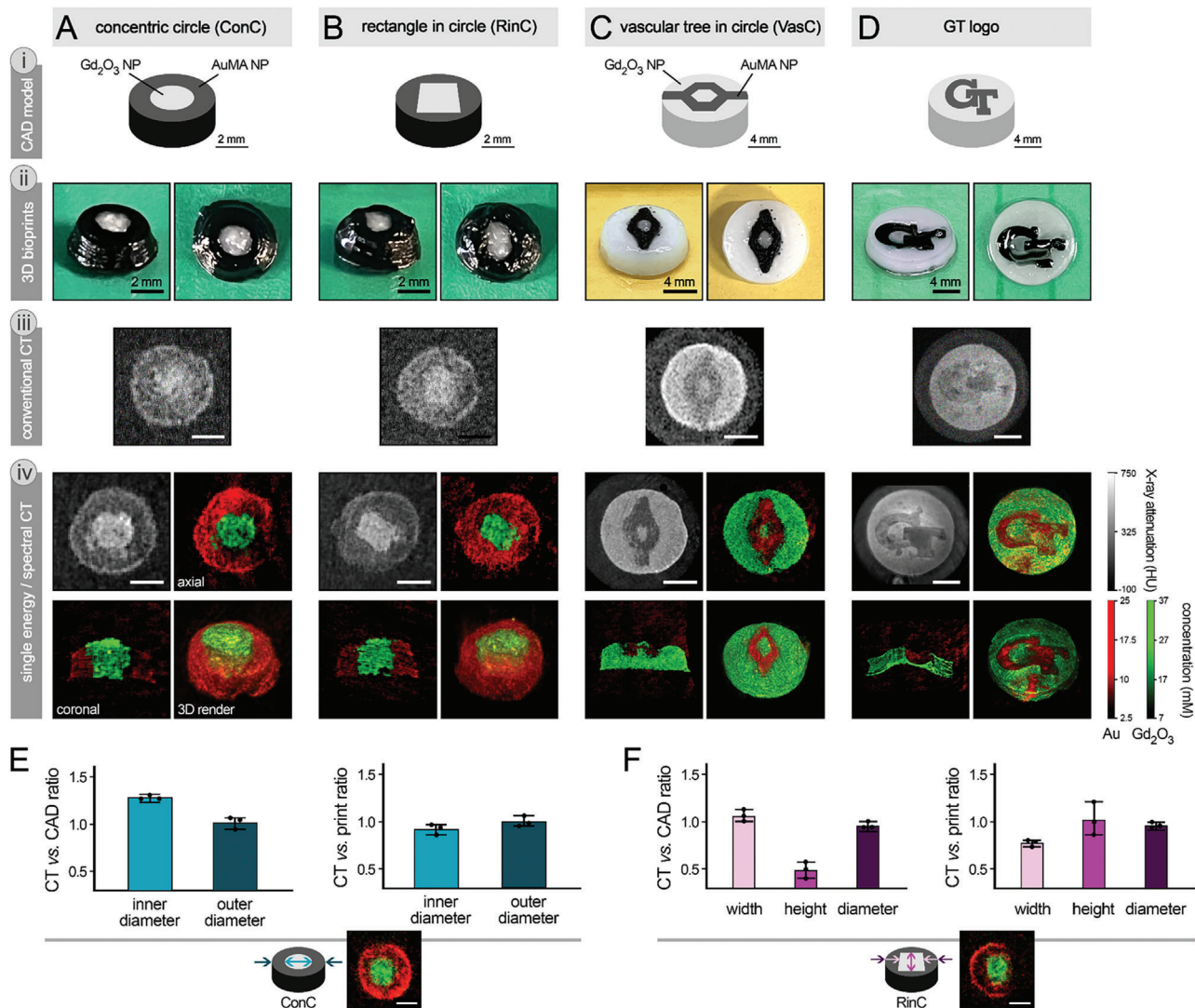
Figure 4. Spectral photon-counting computed tomography (PCCT) of bioprinted constructs of varying geometries, containing multiple contrast agents and their quantitative analysis. Four different scaffold geometries were printed, including an A) concentric circle (ConC), B) rectangle in circle (RinC), C) vascular tree in circle (VasC), and D) Georgia Tech (GT) logo. For each scaffold geometry (A–D), row (i) shows the CAD model of the design with Gd_2O_3 NP and AuMA NP bioinks depicted in different regions. Row (ii) shows photos of extrusion-bioprinted constructs from side (left) and axial/top (right) views where Gd_2O_3 bioinks appear white and AuMA NP bioinks appear black. Row (iii) shows conventional CT image slices for each scaffold design, with X-ray attenuation in grayscale (Hounsfield unit, HU). Row (iv) shows the lowest-energy bin PCCT axial slice (top left) in grayscale (HU) along with axial (top right) and coronal (bottom left) slices of the color-coded Gd (green) and Au (red) decomposed images, as well as a 3D rendering (bottom right). Material map slices are windowed according to the color bars on the far right of this figure. E,F) Fidelity quantification based on the PCCT imaging of E) ConC and F) RinC designs, obtained by normalizing the dimensional measurements in PCCT images by those in the CAD file (left), or by those in the bioprinted construct (right) (n = 3 per group). Insets show representative PCCT images used for the quantifications. Scale bars in (A) and (B) and (E) and (F) show 2 mm and in (C) and (D) show 4 mm. All concentration values are in mM.

(printed with Gd_2O_3 NP bioink) compared to the CAD design (ratio of 1.29 ± 0.01), while it was consistent with the inner diameter measurement in the printed constructs (ratio of 0.92 ± 0.03). The outer diameter in ConC design (printed with AuMA NP bioink) showed a close agreement with both the CAD design (1.02 ± 0.04) and the measured value in the bioprints (1.00 ± 0.03) (Figure 4E). These results indicate that for the concentric circles (ConC) geometry, PCCT imaging did not generate significant error in the structural dimensions of bioprinted constructs, confirming the adequate spatial resolution of the technique for

future quantitative applications. The RinC group also showed an adequate level of fidelity, overall, with width, height, and outer diameter measurements in PCCT matching those of the bioprinted samples (ratios of 0.78, 1.02, and 0.96 for the width, height, and diameter, respectively) (Figure 4F). While the width ratio between PCCT and print showed notable deviation (0.78 ± 0.02), the width ratio between CT and CAD design approached 1.00 (1.06 ± 0.04), suggesting that the PCCT signal closely recapitulated the intended design parameters. There was some significant deviation in the rectangle height measurement between
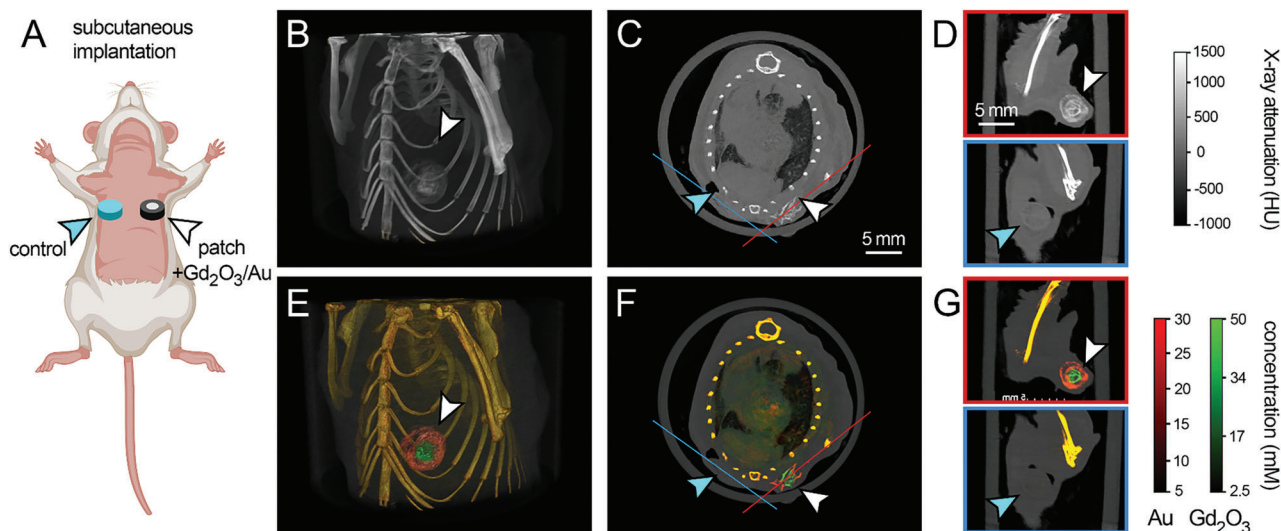
Figure 5. Spectral photon-counting computed tomography (PCCT) imaging of subcutaneous implants in mice to track the location of bioprinted constructs and quantify the concentration of Gd_2O_3 and AuMA NP contrast agents in the scaffolds. A) Wild type mice were bilaterally implanted post-mortem with a bioprinted disc-shape construct containing no contrast agent (control, right side of the chest, the blue arrows) and a bioprinted concentric circle (ConC) implant containing Gd_2O_3 and AuMA NP contrast agents (left side of the chest, the white arrows). B–D) Grayscale PCCT images from a single-energy bin, including a 3D rendered image (B), axial slice (C), and two oblique slices through the implanted constructs (top and bottom) (D). Images are shown in Hounsfield unit (HU) as displayed on the far-right side (−1000 to 1500 HU). E–G) Color-coded images of Gd (green) and Au (red) material basis maps, including a 3D rendered image (E), axial slice (F), and two oblique slices through the implanted constructs (G). Au and Gd maps are shown in mM concentration. Each map was windowed according to the color bars to the right of the decomposed images and then combined as a composite RGB image. Note that the bones appear yellow in the decomposed images. Blue and white arrows point to the control and ConC implants. Scale bars show 5 mm in all images.

CT and CAD (0.49 ± 0.05), which was also noticeable in the photos of printed constructs (Figure 4B,ii). This may be attributed to possible errors in the movement trajectory of extrusion printhead and over/under extrusion of the ink. The process of embedding printed crosslinked constructs in agar, as well as possible swelling of constructs post printing could have also contributed to the structural changes in bioprints.[87,88]

We next evaluated the suitability of generated 3D CT signal from bioprinted geometries to perform quantitative volumetric fidelity analysis[89] by directly superimposing the CT signal to the 3D CAD design (Figure S6, Supporting Information). Quantified signed differences and pass/fail analysis for 3D printed mesh structures, containing AuMA NPs, showed small deviations of the CT signal from the CAD design (Figure S6C,D, Supporting Information). While the signed distance method yields a wider range of interpretations, the pass/fail approach allows for an absolute analysis of areas that contain the greatest amount of error when compared to the design. These 3D measurements would be a great complementary step, in addition to the 2D fidelity measurements presented earlier (Figure 2), as a systematic holistic approach that allows detection of the defects/errors that may occur during and/or post bioprinting processes. The implementation of this methodology into future bioprinting workflows provides a new outlet for qualitative and quantitative evaluation of the bioprinting accuracy and adjusting the design and printing parameters accordingly.[89]

Taken together, the in vitro PCCT results in this study (Figure 4) support the feasibility of design and implementation of more complex structural and functional features within bioprinted implants, such as vascular structures, cellular compo-

nents, and drug eluting features, and enabling their noninvasive, quantitative tracking via PCCT. These are key areas for continued development of the next generation of precision and personalized regenerative medicine treatments. Such advanced CT-visible scaffolds could be used to treat a variety of diseases, including ischemic heart injuries (i.e., cardiac patch devices[90-92]).

Following the in vitro PCCT analysis of bioprinted constructs with varying geometries, we examined the use of spectral PCCT for the detection and quantification of contrast agent-laden 3D bioprinted constructs implanted in an animal model (**Figure 5**). Post-mortem C57BL6 mice were bilaterally implanted (subcutaneous) with printed disc-shaped empty constructs (control) and ConC constructs loaded with multiple contrast agents, on the right and left torso of the mouse, respectively (Figure 5A). Small animal spectral PCCT imaging enabled the detection and quantification of Gd_2O_3 and AuMA NP contrast agents with minimal apparent false signal in the control construct (Figure 5B–G). This is while the control constructs lacking a contrast agent could not be detected (Figure 5B–D). PCCT imaging of bioprinted constructs (Figure 5E–G) markedly enhanced the discernment of construct location compared to image contrast generated from X-ray attenuation differences in conventional CT image slices (Figure 5B–D). Of note, the quantified ranges of Au and Gd_2O_3 reagents within the implanted scaffolds (5–30 mM and 2.5–50 mM, respectively) were in close agreement with those measured for Au and Gd_2O_3 NPs in the in vitro assays for the ConC design (Figure 4, 2.5–25 mM and 7–37 mM, respectively). The bone tissue appeared yellow in the decomposed images since calcium, which was not included as a basis material, was represented as a sum of the Gd and Au bases.

ADVANCED
SCIENCE NEWS

www.advancedsciencenews.com

**ADVANCED
HEALTHCARE
MATERIALS**

www.advhealthmat.de

Spectral PCCT was able to discriminate structural features loaded with different NP contrast agents within the bioprinted constructs by leveraging photon-energy dependent differences in the X-ray attenuation of Au (AuMA NPs) and Gd (Gd_2O_3 NPs). This is achieved using photon-counting detectors, which sort the detector-incident photon events using different configurable energy thresholds. In contrast, conventional CT acquisitions were unable to discern between Au and Gd_2O_3 content due to the inability of traditional energy integrating detectors to discern incident photon energies.

Future studies will explore new encapsulation methods,[93] as well as new, more effective chemical conjugation methods with the polymer (e.g., GelMA) matrix[94,95] to further enhance the contrast agent retention within the printed structures. Future work could also explore the possibility of incorporating/co-encapsulation of therapeutic molecules, together with CT contrast agents, as a novel, indirect, and quantitative method to monitor drug release from implants. CT reagent could further be utilized to track transplanted cells and/or genetic materials within the bioprinted constructs,[96] which could significantly increase the impact of these systems particularly in the regenerative medicine applications. Studying the CT visibility of these engineered implants for longer time periods in vivo, and various disease-specific animal models, would be of great importance. More in-depth SEM and energy dispersive spectroscopy (EDX) analyses in the future works would generate important insight into the pore structure/connectivity and NP distribution within various bioink constructs. While cell culture assays on the developed CT-visible bioinks indicate adequate levels of biocompatibility, future studies could provide more in-depth and tissue-specific bioactivity of these materials. Simultaneous bioprinting of viable cells and contrast agents can create functional, patient-specific implants with significantly enhanced potential for clinical applications. Finally, for the NP systems used in bioink formulations, pharmacokinetics, biodistribution, clearance, and toxicity of NPs should be carefully examined prior to the implementation of CT-visible bioprinted scaffolds into clinical studies.[97,98] Depending on the size of contrast agents, their clearance could occur through the kidney (<5 nm, e.g., Omnipaque, Gadavist, and Aurovist (Au NP) used in this study[99,100]), liver (20–100 nm, e.g., Gd_2O_3, Au, and AuMA NPs[101,102]), and eventually elimination by the mononuclear phagocytic system (MPS) in lymph nodes and the spleen (>200 nm, e.g., Iod-loaded liposome NPs[103]).

3. Conclusions

In this study, bioinks comprising molecular (Iod and Gd) and NP (Iod-loaded liposome, Au, AuMA, and Gd_2O_3) CT contrast agents were used to 3D bioprint hydrogel scaffolds of varying geometries at adequate levels of structural fidelity. In-depth analysis of the release behavior of contrast agents from the constructs demonstrated the poor retention of molecular agents; hence, these types of clinically used reagents are not optimal for monitoring of bioprinted constructs. NP contrast agents, on the other hand, provided a stable and robust signal over time durations that are suitable for most clinical applications. Printed NP contrast agent-laden constructs were evaluated by conventional CT versus spectral PCCT in vitro and in a subcutaneous mouse model. Constructs printed with multiple bioinks containing distinct contrast

agents (Gd_2O_3 and AuMA NPs) showed distinguishable, robust PCCT signal, which enabled noninvasive monitoring of the implanted scaffold position and quantification of contrast agent concentrations. This study, therefore, demonstrates the feasibility of design and developing a novel theranostic platform with potential for clinical applications in treating a variety of diseases, including cardiovascular disease (i.e., as CT-visible cardiac patch). The integration of multi-material 3D bioprinting together with functionalized nano-biomaterials and PCCT imaging provides a robust means for tissue engineers to advance the field toward the development of next-generation precision and personalized medicine platforms.

4. Experimental Section

Preparation of GelMA Bioinks: The GelMA used in this study was synthesized using a similar protocol as in previous studies.[55,56,59] Briefly, PBS was used to dissolve gelatin powder at 10% (w/v) at 50 °C, with methacrylic anhydride (MA, Sigma) added dropwise at the same temperature over a 3-h period. To stop the methacrylate reaction, warm PBS was added to the solution, followed by dialysis in deionized (DI) water for 1 week at 40 °C. During this process, the water was changed three times a day. Subsequently, the mixture solution was lyophilized and stored at −20 °C in a dark environment. Stock solutions of 20% GelMA were prepared by the reconstitution of lyophilized GelMA in PBS with 1% w/v Irgacure (Sigma).

Preparation of CT Contrast Agents: Two sets of CT contrast agents, that is, molecular and NP contrasts, were used in this study. Molecular contrast agents included gadolinium (Gd) (Gadavist, Bayer HealthCare Pharmaceuticals Inc.) at molecular weight of 604.7 g mol^{-1} ($\approx$1.2 nm) and iodine (Iod) (Omnipaque 350, GE Healthcare Inc.) at molecular weight 821.14 g mol^{-1} ($\approx$1.2 nm). Nanoparticle (NP) contrast agents included Gd_2O_3 NP (Nanostructured & Amorphous Materials Inc.) in the form of power with a molar mass of 362.5 g mol^{-1}, gold (Au) NP (VivoVist, Nanoprobes) in 1015.40 mm concentration and 15 nm particle size, and methacrylated Au (AuMA) NPs (preparation described below) (Table 2).

Preparation of GelMA Bioinks Laden with Various CT Contrast Agents: Printing syringes of bioinks laden with CT contrast agents, including Iod, Gd, Gd_2O_3 NPs and Iod-loaded liposome nanocapsules, were prepared using 1.8 mL of 20% GelMA and 1.2 mL of the corresponding contrast agent stock solution. Thus, the final concentration of GelMA was adjusted at 12% and the concentration of Iod, Gd, Gd_2O_3 NPs, and Iod-loaded liposomes in the bioinks were adjusted at 49.8, 41.6, 22.3, and 49.8 mm, respectively (Table 2).

To prepare the GelMA bioink containing Au NP contrast agents, a stock solution of 33.33% GelMA was prepared by the reconstitution of lyophilized GelMA in PBS with 0.83% w/v LAP (Sigma). Printing syringes of Au NP were prepared using 1.8 mL of 33.33% GelMA and 1.2 mL of Au NP stock solution. Final concentration of GelMA and Au NP were 20% (w/v) and 20.2 mm, respectively (Table 2). The concentrations of all contrast agents were selected based on the standard curves of X-ray attenuation for each agent, to achieve a clinically relevant level of CT contrast ($\geq$150 HU).

Synthesis of AuMA NPs—Preparation of GelMA Bioinks Containing AuMA NPs: AuMA NPs were synthesized by surface functionalization of bare Au NPs, prepared by the citrate reduction method,[104] with mercaptosuccinic acid (MSA) which was subsequently covalently-linked to 2-aminoethyl methacrylate (AEMA, 90%, $C_6H_{11}NO_2 \cdot HCl$, Sigma-Aldrich) using carbodiimide/succinimide chemistry, as previously described in detail.[53] Briefly, 0.5 mmol of MSA-functionalized Au NPs (AuCOOH NPs) were added to 200 mL ethanol (80% v/v) containing 1.44 g 1-ethyl-3-(3-dimethylaminopropyl) carbodiimide hydrochloride (EDC, Sigma-Aldrich) and 0.65 g N-hydroxysulfosuccinimide (NHS, Sigma-Aldrich). The resulting mixture was then added with another 200 mL ethanol (80% v/v), containing 0.495 g fully dissolved AEMA, such that the molar ratio of

Table 3. Summary of the bioprinting parameters used in this study to print various bioink groups.

Bioink	GelMA bioink (1)	GelMA bioink (2)	Iod bioink	Gd bioink	Gd$_2$O$_3$ bioink	Au bioink	AuMA bioink	Iod-liposome bioink
[GelMA] wt%	12%	20%	12%	12%	12%	20%	20%	12%
Contrast agent	—	—	Molecular	Molecular	NP	NP	NP	NP
Print temp [°C]	24	24	19	20	25	20.5	20.5	20.5
Print speed [mm^{-1}s]	6	6	5	5	5	5	5	5
Print pressure [kPa]	55–90	105–120	200	170	140–200	200	90–130	80
Crosslinking intensity [mW cm^{-2}]	7	30	7	7	7	30	30	7
Crosslinking time [min]	4	4	4	4	4	4	4	4

NP: nanoparticle. GelMA: gelatin methacrylate. Iod: iodine. Gd: gadolinium. Au: gold. AuMA: methacrylated gold.

Au:EDC:NHS:AEMA was 1:15:6:6. The mixture was vigorously stirred under nitrogen protection for 24 h at room temperature to obtain AuMA NPs. After the reaction, AuMA NPs were collected by centrifugation at 8400g for 30 min and washed thrice with DI water. The final AuMA NP stock solution was concentrated to 101 mM as verified by inductively-coupled plasma optical emission spectroscopy (ICP-OES).[104]

To prepare the AuMA NP bioink, a stock solution of 40% GelMA was prepared by the reconstitution of lyophilized GelMA in PBS and 2.8 mL of a 1.25% w/v LAP solution. Subsequently, 0.7 mL of AuMA NP stock solution (101 mM, as explained above) was added. Thus, the final concentrations of GelMA and AuMA NPs in the bioink were 20% and 10 mM, respectively (Table 2). The concentration of AuMA NP was selected based on the standard curve of X-ray attenuation for Au, to achieve a clinically relevant level of CT contrast ($\geq$150 HU).

Synthesis of Iod-Loaded Liposome Nanocapsules: The Iod-loaded liposomes were prepared using the thin film hydration method. Briefly, a lipid mixture consisting of L-α-phosphatidylcholine type XVI-E from fresh egg yolk (Egg-PC) (Sigma Aldrich) and cholesterol (Sigma Aldrich) in a 70:30 molar ratio was dissolved in chloroform at a lipid concentration of 50 mg mL^{-1} in a flat bottom glass vial. The chloroform was slowly evaporated under vacuum in a desiccator overnight to obtain a homogeneous and thin lipid film in the bottom of the vial. A hydration solution was prepared by mixing an Iod solution (1 mM) with 10× PBS buffer to reach a final concentration of 1× PBS. The hydration solution was heated to 37 °C prior to be used to hydrate the lipid film with a lipid concentration of 40 mM. The lipid film was left for 120 min at 37 °C and gently stirred for 30 min using a vortex. The lipid solution was then sonicated in a bath for an extra 30 min at 37 °C. The multilamellar vesicle suspension generated by hydration of the lipid film was then sequentially extruded with ten passes through a 400 nm Nucleopore membrane (Whatman, Buckinghamshire, UK) using an Avanti mini extruder (Avanti Polar Lipids Inc., Alabama, US). The resulting solution was then centrifugated to remove the buffer containing non-encapsulated Iod and recovered in 1× PBS buffer. An Amicon ultra centrifugal filter (100 kDa) was used to perform three washes with fresh PBS 1× and remove the rest of non-encapsulated Iod. The solution of liposomes prepared was then kept at 4 °C until use.

Dynamic Light Scattering Analysis of Liposome Nanocapsules: To determine the diameter distribution of the Iod-loaded liposome NPs synthesized in this study, dynamic light scattering (DLS) technique using a ZetaSizer Nano ZS instrument (Malvern Instruments Ltd., Worcestershire, UK) was used as previously described.[105,106]

STL Design Preparation and Bioprinting of Tissue Constructs Containing Single Contrast Agents: The 3D CAD design of a disk-shaped construct (5 mm in diameter and 1.5 mm in height) was designed using Fusion 360 (Autodesk). The structure was exported as an STL file and placed on Repetier Host (Hot-World GmbH & Co) for slicing. The resulting g-code with instructions to print four replicates of the design was loaded into a microextrusion bioprinter (BioX, CELLINK). Printing syringes containing the prepared functionalized bioinks (laden with one of the CT contrast agents, prepared as above) were installed i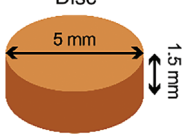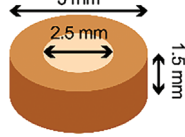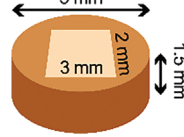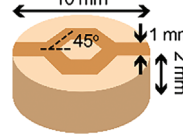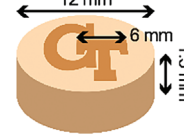nto a temperature-controlled printing head. A 27-gauge tapered needle was used for micro-extrusion. Printing temperature, pressure, and speed were optimized for each bioink until appropriate extrusion and layer depositing was observed (**Table 3**). Following the printing step, AuMA—GelMA constructs were photocrosslinked using UV light at 30 mW cm^{-2} for 2 min on each side. Constructs prepared with other bioinks were subjected to the same treatment with a UV intensity of 7 mW cm^{-2} (Table 3). Post crosslinking, constructs were either freshly used (for release studies) or were embedded in 3% agar and stored at −80 °C freezer to inhibit potential diffusion of contrast agents and preserve the printed tissue structure for further evaluation (CT imaging).

STL Design Preparation of Tissue Constructs Containing Multiple Contrast Agents: Three disk-shaped constructs were designed in Fusion 360 (Autodesk). These designs consisted of a concentric circle (ConC), a rectangle in circle (RinC), and a vascular tree in circle (VasC) (**Table 4**). The ConC and RinC designs were 5 mm in outer diameter, 1.5 mm in height, and used Gd$_2$O$_3$ in the inner and AuMA NP in the outer part. The inner circle of ConC was 2.5 mm in diameter. The rectangle in RinC was centered in the disk with dimensions of 2 mm × 3 mm (Table 4). The VasC design consisted of a vascular tree, printed with AuMA NP bioink, embedded in the center of a disk, printed with Gd$_2$O$_3$ bioink. The disc was 10 mm in diameter and 2 mm in height. The vascular tree component had inlet/outlet vessels each at 1 mm diameter and 1.75 mm length, bifurcating at a 90° angle into the middle channels at 1 mm diameter and 2 mm length (Table 4).

Extrusion-Based Bioprinting of Tissue Constructs: Both components of each design, as described above, were exported separately as STL files, and aligned back together on Repetier Host (Hot-World GmbH & Co) for slicing. A g-code with instructions to print a single replicate at a time was loaded into a microextrusion bioprinter (BioX, CELLINK). The AuMA NP and Gd$_2$O$_3$ bioink syringes were placed in temperature-controlled printing heads with a 27-gauge tapered needle. Printing temperature, pressure, and speed were optimized until both bioinks showed appropriate extrusion, layer deposition, and interaction with one another (Table 3). Optimized parameters for the ConC and RinC designs were the following: AuMA NPs— 20% GelMA (20.5 °C, 5 mm^{-1}s, 90 kPa) and Gd$_2$O$_3$ NPs—12% GelMA (25 °C, 5 mm^{-1}s, 140 kPa). After printing, all replicates were immediately photocrosslinked with UV light at 30 mW cm^{-2} for 2 min on each side. All constructs were embedded in 3% agar immediately after crosslinking to avoid possible diffusion/leakage of contrast agents. Embedded samples were stored at −80 °C until use (imaging).

DLP-Based Bioprinting: A model of the GT logo was derived from official vector graphics provided by Georgia Tech, which were then transformed into an SVG file format and imported into Fusion360 (Autodesk) as previously described,[107-109] to generate a 3D STL file of the logo (dimensions reported in Table 4). A Lumen X+ DLP bioprinter (CELLINK) was used to fabricate high-resolution constructs with complex embedded geometry, that is, the GT logo. A custom formulated bioink (CytoInk6000)[107,108,110] that was specifically tailored was used to produce high fidelity DLP bioprints. Briefly, 10% (w/v) of porcine GelMA (Sigma and in-house methacrylated), 10% (w/v) cold water fish gelatin (Sigma), and 2.5% (w/v) polyethylene glycol dimethacry-

2302271 (12 of 18)

Table 4. Summary of the 3D scaffold geometries used in this study.

Construct geometry	Disc	ConC	RinC	VasC	GT logo
Diameter, d [mm]	5	5	5	10	12
Height, h [mm]	1.5	1.5	1.5	2	1.5
Inner part dimensions [mm]	—	Inner diameter: 2.5 Height: 1.5	Rectangle: 2 × 3 Height: 1.5	Vessel diameter: 1 Height: 2 Bifurcation angle: 45°	"T" width: 6 Height: 1.5
Bioink(s) used	All single contrast agents	Outer: AuMA NP Inner: Gd_2O_3 NP	Outer: AuMA NP Inner: Gd_2O_3 NP	Outer: Gd_2O_3 NP Inner: AuMA NP	Outer: Gd_2O_3 NP Inner: AuMA NP
[bioink] [%]	12% GelMA (Iod, Gd, Gd_2O_3, Iod-liposome) 20% GelMA (Au, AuMA)	20% GelMA (AuMA) 12% GelMA (Gd_2O_3)	20% GelMA (AuMA) 12% GelMA (Gd_2O_3)	20% GelMA (AuMA) 12% GelMA (Gd_2O_3)	10% GelMA, 10% CWF gelatin, 2.5% PEGDMA6000 (AuMA) 12% GelMA (Gd_2O_3)

NP: nanoparticle. GelMA: gelatin methacrylate. I: iodine. Gd: gadolinium. Au: gold. AuMA: methacrylated gold. CWF gelatin: cold water fish gelatin. PEGDMA6000: polyethylene glycol dimethacrylate (PEGMDA) at 6000 molecular weight:

late (PEGDMA6000) (Sigma, in-house methacrylated) was combined and 1% (w/v) of lithium phenyl-2,4,6-trimethylbenzoylphosphinate (LAP) was added to serve as a photoinitiator and 1× pen/strep to prevent contamination. The reagents were suspended in PBS and incubated overnight at 37 °C, protected from light. The bioink was then adjusted to pH of ≈7.5 and 1.5 mM of Tartrazine was added, to serve as a photoabsorber. The final bioink mix was incubated at 37 °C for another 3 h, then stored at 4 °C until use in downstream applications. Where Gd_2O_3 NPs or AuMA NPs were necessary to add to the bioink, these were resuspended in the PBS prior to addition to the dry reagents, to maintain the above listed ratios. As prepared, and if protected from light at 4 °C, the bioinks were stable with minimal bioprinting capability degradation for at least a month.

Due to the limitation of DLP bioprinting to use only one bioink, plan was to print the more complex component, that is, the GT logo, and then cast the rest of the disc construct using a printed model. The GT logo model was imported into the Lumen X+ slicer software to generate the layer-by-layer printable directions. The AuMA NP bioink (in CytoInk6000 formulation, Table 4) was used to print the logo. Also, a 20 mW cm^{-2} 405 nm blue light, 7 s per layer, with 14 s for first layer burn-in were used as the bioprinting parameters for all bioinks done on the Lumen X+. The completed GT model from bioprinted runs were recovered from the stage and incubated overnight in a 50 mL conical tube, filled with 1× PBS and 1× pen/strep to remove the non-crosslinked bioink. Subsequently, the GT logo was positioned into a circle-shape mold (12 mm diameter, 1.5 mm height) and cast with the Gd_2O_3 NP bioink (in 12% GelMA, Table 4), followed by crosslinking for 2 min at 20 mW cm^{-2} under UV light. The ring mold was then removed, and the completed constructs were placed in a 50 mL conical tube (Corning) containing 1× PBS with 1× pen/strep to remove any excess bioink. Constructs were subsequently embedded in 3% agar and stored at −80 °C until use, as above, to preserve the contrast agent distributions within the structures.

Bioprinting Fidelity Assessment: Printability of various bioinks was evaluated via, first, characterizing their micro (strand)-scale fidelity on two-layer lattice structures created via extrusion bioprinting (BioX, CELLINK). Strand diameter ratio (r_d), strand angle ratio (r_α), strand uniformity ratio (r_U), and inter-strand area ratio (r_A) was measured as representative of strand-level fidelity using the protocol established before.[19,55,59,108] In this method, r_d determines the accuracy in the printed strand diameter, r_α measures the precision in the angle between the two layers of strands, r_U quantifies the uniformity (straightness) of the extruded strands, and

r_A quantifies the surface area variation of the quadrilateral areas created by four crossing strands, and. These ratios were obtained by dividing the measured (experimental) values by the theoretical value for each parameter in the CAD design using the following equations:

$$r_d = \frac{\text{diameter of printed strand}}{\text{diameter of designed strands} = 0.3 \text{ mm}} \tag{1}$$

$$r_\alpha = \frac{\text{angle between two printed strands}}{\text{designed angle between strands} = 60°} \tag{2}$$

$$r_U = \frac{\text{length of printed strand}}{\text{length of designed strand} = 1.1 \text{ mm}} \tag{3}$$

$$r_A = \frac{\text{surface area between printed strands}}{\text{surface area between designed strands} = 1 \text{ mm}^2} \tag{4}$$

Therefore, calculated values approaching 1 would suggest a 100% accuracy/fidelity in bioprinted strands and deviations from 1 would represent the error in micro-fidelity.[19,55,59,108] Ratio calculations were performed using measurements from each replicate ($n = 5$) on ImageJ. We used 4× optical images to measure r_d, r_α, and r_A using the angle, freehand selection, and straight-line tools, respectively, on ImageJ. The 1.25× optical images were used to measure r_U by tracing the center of printed strands with the freehand line tool. In each replicate, measurements of 6 different strands were taken to calculate r_U (three vertical and three horizontal segments), and 12 measurements were used to calculate r_d, r_α, and r_A.

We next quantified bulk (macro-scale) fidelity of bioprinted constructs, performed on the disk-shaped scaffolds prepared via extrusion bioprinting (BioX, CELLINK). Bright field optical images of the complete printed constructs were taken using a smartphone camera. Disk diameter (D) was measured on ImageJ using the straight-line tool by taking four diameter measurements in vertical, horizontal, and diagonal directions. The r_D ratio was calculated by dividing the measured parameter to that in the CAD design

$$r_D = \frac{\text{diameter of printed disc}}{\text{diameter of designed disc} = 5 \text{ mm}} \tag{5}$$

Similar to the micro-scale fidelity, a r_D ratio of 1 indicated optimal bulk printing fidelity. Four replicates ($n = 4$) were measured both before and after they were subjected to UV photocrosslinking.

Mechanical Characterization of Bioprinted Constructs: GelMA-based printouts were crosslinked by UV exposure from both top and bottom sides by flipping the samples (identical top and bottom crosslinking). A constant light intensity of 7 mW cm^{-2} and crosslinking duration of 2 min was used for all 12% GelMA based bioinks. For 20% GelMA-based bioinks, the crosslinking duration stayed the same, but the intensity was raised to 20 mW cm^{-2}. The modulus of elasticity (E) of printed samples were measured using the microindentation test (Mach-1 mechanical testing system, Biomomentum Inc., Quebec, Canada) as previously described.[46,56,107-109] Briefly, a 500 μm spherical probe was employed to indent the surface of bioprinted samples with different compositions ($n = 6$), with the indenting depth of 100 μm at a speed of 2 μm s^{-1}. The force–displacement unloading curves were recorded and used to calculate the stiffness of the sample (S) from the linear tread line slope (initial 5–20%), and the reduced elastic modulus (E_r) was derived following the equation[111]

$$E_r = \frac{\sqrt{\pi}}{2\beta} \frac{S}{\sqrt{A(h_c)}} \tag{6}$$

where β is a constant and equals 1 in these tests, $A(h_c)$ is projected contact area at the contact depth of h_c and can be obtained from the following equation:

$$A(h_c) = 2\pi R h_c - \pi h_c^2 \tag{7}$$

where

$$h_c = h_{max} - \varepsilon \frac{P_{max}}{S} \tag{8}$$

where h_{max} and P_{max} are the peak unloading displacement and unloading force, respectively, and ε is a constant with a value of 0.75 for the spherical indenter used here.[112] The elastic modulus, E, can be calculated using the following equation[111]

$$\frac{1}{E_r} = \frac{(1-\nu^2)}{E} + \frac{1-\nu_i^2}{E_i} \tag{9}$$

where ν is the Poisson's ratio of tested material with a value of 0.5, and ν_i is 0.5 for the indenter tip material. E_i represents the elastic modulus of the probe, with a value of 2 GPa.

Rheological Measurements of Gel Solutions: Rheological parameters of hydrogel samples were measured using an AR 2000 rheometer (TA Instruments) with a 25-mm parallel plate geometry. For this purpose, 800 μL of each bioink solution was pipetted onto the bottom plate of the rheometer and the gap size was set at 400 μm. Excess hydrogel solution was removed from the rheometer with Kimwipes (Kimtech). A solvent trap was used to prevent evaporation during experiments. Time sweep and temperature sweep assays were performed on the 12% GelMA, 20% GelMA, 12% GelMA + Gd$_2$O$_3$ NP, and 20% GelMA + AuMA NP bioink groups. Time sweep experiments were conducted for 10 min, at 1% strain and 1 Hz frequency as the evolution of the storage moduli (G') and the loss moduli (G'') were observed. For time sweep experiments, a constant temperature of 24 °C (for 12% GelMA), 24 °C (20% GelMA), 25 °C (12% GelMA + Gd$_2$O$_3$ NP), and 20.5 °C (20% GelMA + AuMA NP) were applied. Temperature sweep measurements were conducted to determine the G' and G'' from 15 to 40 °C at the rate of 1 °C min^{-1}, covering all printing temperatures used in this study. Hydrogel solutions were sheared at 1 Hz frequency and 1% strain.

Scanning Electron Microscopy Imaging: A disc-shape scaffold containing a vascular tree was printed and examined under vacuum in the scanning electron microscope (Axia ChemiSEM, Thermo Fisher, Waltham, MA). The operating voltage was 8 kV. Specimen preparation included drying the construct in ambient air and temperature and sputter coating the surface with 10–12 nm gold-palladium alloy for conductivity, using a Quorum 150 V ES Plus (Quorum Technologies, Laughton, East Sussex, United Kingdom). Quantitative SEM analysis for pore size distribution was conducted using $n = 3$ replicates. Clear pores with distinguishable walls and structure were selected and used for the pore size distribution analysis. For each pore, measurements of diameter were performed from five distinct angles for a total of 750 data points per SEM image. The data across samples were compiled. Analyses included a frequency distribution of pore diameter and a nonlinear regression curve for a Gaussian distribution.

Biocompatibility Assays: 100 μL of each bioink solution (12 and 20% GelMA without NPs, 12% GelMA + Gd$_2$O$_3$ NP, and 20% GelMA + AuMA NP) were cast into wells of 24-well plates and crosslinked via UV light, resulting in disc-shape constructs at approximate height of 0.5 mm and diameter of 14 mm. The 12% GelMA bioinks (with and without Gd$_2$O$_3$ NPs) were crosslinked at 7 mW cm^{-2} for 45 s for the top surface and 45 s for the bottom surface. The 20% GelMA bioinks (with and without AuMA NPs) were crosslinked with UV light with intensity of 20 mW cm^{-2} for 45 s on the top surface and 45 s on the bottom surface. After crosslinking, constructs were washed with sterile PBS (3×2 min) and kept in PBS until cell culture.

Human umbilical vein endothelial cells (HUVECs) (ATCC) were cultured in HUVEC media and media was changed every 3 days. At 90% confluency, cells were passaged and seeded onto the bioprinted constructs. HUVECs were seeded onto the surface of the bioink substrates at 5×10^3 cells per well. For the AuMA NP group, HUVECs were seeded at 1×10^4 cells per well. To assess cell viability using AlamarBlue assay, at different time points (days 1, 3, and 7), culture media was aspirated from each well and replaced with fresh media containing AlamarBlue reagent (1:9 volume ratio).[113-115] After a 4-h incubation, 100 μL of incubated reagents were transferred to a 96-well plate ($n = 3$ per group per time point). AlamarBlue reduction percentage was calculated based on the different light absorption at 550 and 600 nm wavelengths, using a microplate reader machine (BioTek Instruments, US). In addition, Live/Dead assay (Millipore) was performed at day 7 of culture by mixing a 1:1 ratio of cell culture medium and PBS and adding 5 μL Calcein AM, and 20 μL propidium iodide per 24 mL. After aspirating media in each well, 1 mL of dye solution was added to each well and incubated for 30 min. Following incubation, scaffolds were washed with culture media and imaged via a fluorescence microscope (DFC3000 G, Leica) at 20× magnification.

In Vitro Examination of Contrast Agent Retention Profile in Bioprinted Constructs—Micro-CT Imaging: Standard curves of X-ray attenuation for all contrast agents (Iod, Gd, Gd$_2$O$_3$ NPs, Au NPs) were measured and plotted with a conventional laboratory micro-CT (μCT-40, Scanco Medical AG) with serial dilutions of each contrast agent, including 0, 5, 16, 25, 40, 50, 70 mm, in DI water. Subsequently, disc-shape constructs of dimensions ($d = 5$ mm and $h = 1.5$ mm) were bioprinted using contrast agent-laden bioinks, according to the parameters listed in Tables 2–4, using the Bio X printer (CELLINK). To print the constructs, bioinks were formulated at adequate contrast agent concentrations to ensure obtaining clinically relevant X-ray attenuation for soft tissue imaging (>150 HU, based on the standard curves).[57] Specifically, the concentrations used were 42 (Iod), 50 (Gd), 20 (Au NP), and 22 mm (Gd$_2$O$_3$ NPs).

All molecular contrast agent (Iod and Gd) bioinks were printed in four replicates ($n = 4$) for each timepoint of the release study, that is, $t = 0$, 0.5, 1, and 2 h. Similar approach was used to quantify the release of NP contrast agents from printed constructs; however, since the NPs were sought to have greater retention and slower release than the molecular agents, the timepoints studied for NPs were extended to $t = 24$ and 504 h (3 weeks) ($n = 4$). Following bioprinting and crosslinking, all constructs were immediately submerged in 2 mL of PBS in a 24-well plate and either underwent static conditions (no movement) or dynamic conditions (on rocking plate at 40% intensity). At each time point, the samples were removed from solution, rapidly placed in a falcon tube with 2 mL of solidified 3% agar at the bottom, and immediately embedded with liquid 3% agar. Embedded samples were placed in a dry ice container and transferred to −80 °C to preserve the sample from any further diffusion/release. To quantify the

ADVANCED
SCIENCE NEWS

www.advancedsciencenews.com

**ADVANCED
HEALTHCARE
MATERIALS**

www.advhealthmat.de

release at each given time point, frozen samples were retrieved and immediately imaged via micro-CT (µCT-40, Scanco Medical AG) at 70 kVp tube potential, 36 µm voxel size, 144 µA beam current, and 250 projections at 200 ms integration time.

Spectral PCCT Image Acquisition, Reconstruction, and Material Decomposition: PCCT images of bioprinted multi-contrast agent constructs were acquired via two different PCCT systems. In the first round, PCCT imaging was performed on a custom micro-PCCT imaging system (Duke University),[116] equipped with a SANTIS 1604 CdTe-based PCD from DECTRIS, Ltd. This detector has a pixel pitch of 0.15 mm, a 16×4 cm active area, and four configurable energy thresholds. The system had a MicroFocus X-ray source with a tungsten anode (Thermo Scientific, model PXS10). The object of interest was placed on a stage which was rotated and vertically translated to acquire projection data in a helical trajectory. The source, object, and detector were placed such that the system magnification is ≈2.5. The source was set to a tube voltage of 120 kVp with a tube current of 200 µA. The PCD thresholds were 35, 50, 80, and 86 keV. The lowest energy level was chosen to provide reference data with high photon counts and low noise while the upper thresholds were chosen to surround the characteristic K-edges of Gd (50.2 keV) and Au (≈80.7 keV). For this study, 1200 X-ray projections were taken over a total of three rotations and 25 mm of translation.

PCCT reconstructions were jointly performed with log normalized multi-energy projection data at a voxel size of 75 µm using a multi-channel iterative reconstruction algorithm.[117] This algorithm seeks to solve simultaneously the following optimization problem for all energies e:

$$X = \arg\min_X \frac{1}{2} \sum_e \| RX(e) - Y(e) \|_2^2 + \lambda \| X \|_{BTV} \tag{10}$$

where, X represents the multi-energy tomographic data, Y represents the log-normalized projection data, and R represents the system projection matrix. Noise in the reconstructions was reduced by minimizing the data fidelity subject to the bilateral total variation (BTV) within and between energy levels. BTV was reduced using rank-sparse kernel regression regularization.[117]

The four PCD energy threshold images were decomposed into Gd and Au material basis concentration maps using a post reconstruction decomposition approach.[118] An orthogonal subspace projection was used to enforce a non-negativity constraint on concentration values.[117] The decomposed material maps were saved as RGB, color-coded images and visualized using 3DSlicer (https://www.slicer.org/).

Second round of PCCT imaging was performed (University of Notre Dame) on a commercially available system (MARS-12 and MARS-19, MARS Bioimaging, Christchurch, NZ). This system was equipped with a polychromatic X-ray source operating at 120 kVp, 2.5 mm aluminum filtration, and a photon-counting detector comprising a CdZnTe semiconductor sensor, 2 mm in thickness, bonded to a Medipox3RX chip[119] with a 110 µm pixel pitch and five energy bins in charge-summing mode. The X-ray tube current was 24 µA which corresponded to a photon count rate of 10 photons ms^{-1} for a given pixel to mitigate potential error due to pulse pileup. The image acquisition protocol utilized a helical scan with 720 projections per gantry rotation, a 45 mm field of view, and 250 ms integration time to limit each detector pixel to a mean of 2500 total counts across energy bins. Source-object and source–detector distances were set at 209.8 and 274.8 mm, respectively, resulting in a magnification level of 1.31. Energy thresholds were selected to create five energy bins at 7–30.5, 30.5–43, 43–55, 55–65.5, and 65.5–120 keV. Careful selection of energy bins ensured equal photon counts across bins and leveraged differences in the X-ray attenuation of Au and Gd_2O_3 across the photon energy spectrum, including the K-edge discontinuities of Gd and Au at 50.2 and 80.7 keV, respectively. CT reconstructions were performed with an isometric voxel size of 100 µm and a nominal spatial resolution of 300 µm. Prior to image acquisition, atypical and extreme pixels were selectively masked based on atypical lower and upper thresholds and variances of photon counts.

For the second round of PCCT, material decomposition of multiple contrast agents (Au, Gd_2O_3) was performed using constrained maximum likelihood estimation (MLE) in the image domain, adapting methods previously demonstrated for spatially coincident contrast and tissue compositions.[33] Briefly, MLE was calibrated by an $M \times N$ material basis matrix, where M is the number of energy bins and N is the number of elements or materials to be decomposed. The material basis matrix was established by linear least squares regression of the X-ray attenuation measured in each energy bin versus known concentrations of each material composition in the material phantom. The X-ray attenuation was measured as the mean attenuation within a 12 mm^3 cuboidal volume of interest located at the center of each Eppendorf tube in the phantom images. Elemental volume fractions were estimated from the known concentrations of compositions in the phantom based upon the mass and density of Au, Gd_2O_3 and water. The fractional abundance of materials within a given voxel in the sample phantom was determined using quadprog, a quadratic programming function in MATLAB (v9.9, MathWorks, Inc.) such that solutions to the linear system of equations satisfied prior assumptions of non-negativity and full additivity within each voxel. Following material decomposition, all material volume fractions were scaled to millimolar (mM) concentration using the material basis matrix and linear regression models determined from the phantom.

Volumetric Fidelity Assessment: The DLP bioprinting approach described above was utilized to fabricate a 3D mesh structure at adequate resolution and fidelity, using 20% w/v porcine GelMA (150 bloom, Sigma), 20 mM PEGDMA (Biosciences), 1% w/v (LAP; Sigma), and 1.5 mM Tartrazine (Sigma). AuMA NPs were added to the filtered bioink at a final concentration of 10 nM. A Lumen X+ (BICO; CELLINK) was used to print at least six replicates of mesh geometry, with a random selection of $n = 3$ used for fidelity measurements. Standardized bioprinting parameters were used, accounting for the light absorption reported for gold NPs in the 405 nm range. Specifically, 15 mW cm^{-2} light intensity was used and were crosslinked with each layer in the constructs for 9 s, with a burn-in for the first layer of 18 s.

Following bioprinting, constructs were imaged via micro-CT, as described above and CT scan stacks were imported into FIJI ImageJ. A 3D median filter with a pixel width of 2 was applied to smooth the image surfaces and loaded into 3D viewer mode. Using a threshold of 80, the data were converted to an STL file and imported into the 3D point cloud processing software (CloudCompare, www.cloudcompare.org). Using the software's built-in scissoring tool, the STL file of the scanned scaffold was edited to remove any undesired background areas. Both the scanned object's STL and the corresponding CAD design were then scaled to matching dimensions, registered, and surface deviation calculations were performed. Adapting previous methods, these deviations were illustrated through a signed distance and pass/fail error detection analysis.[89]

Subcutaneous Mouse Implantation of Bioprinted Constructs and PCCT Imaging: To demonstrate quantitative spectral PCCT imaging of 3D bioprinted scaffolds implanted in mice, fresh post-mortem wild-type C57BL/6 mice ($n = 6$) were subcutaneously implanted with non-contrast (empty 12% GelMA, as control) and NP contrast agent-loaded bioprinted constructs in a bilateral fashion within the torso. Implanted mice were placed on a mouse bed for imaging with spectral PCCT settings as described above for imaging bioprinted constructs. The mice were sacrificed after use in other in vivo experiments conducted by colleagues at Emory University (all under active IACUC protocols). Immediately after they were sacrificed, we received the bodies and used them for our imaging studies presented in this article.

Statistical Analysis: Experimental data was processed and expressed using mean values ± SEM. Statistical significance was determined by a t-test, one-way or two-way analysis of variance, and multiple comparisons were performed by ANOVA test using GraphPad Prism with an acceptable significance level of $P < 0.05$. In the entire study, *$P < 0.05$, **$P < 0.01$, ***$P < 0.005$, and ****$P < 0.001$ in comparison to the previous time point for each group.

Supporting Information

Supporting Information is available from the Wiley Online Library or from the author.

**ADVANCED
SCIENCE NEWS**

www.advancedsciencenews.com

**ADVANCED
HEALTHCARE
MATERIALS**

www.advhealthmat.de

Acknowledgements

Conflict of Interest

The authors declare no conflict of interest.

Author Contributions

Data Availability Statement

The data that support the findings of this study are available from the corresponding author upon reasonable request.

Keywords

[1] E. J. Lee, F. K. Kasper, A. G. Mikos, *Ann. Biomed. Eng.* **2014**, *42*, 323.

[2] K. Sharma, M. A. Mujawar, A. Kaushik, *Front. Mater.* **2019**, *6*.

[3] D. S. Kohane, R. Langer, *Pediatr Res* **2008**, *63*, 487.

[4] A. Khademhosseini, N. Ashammakhi, J. M. Karp, S. Gerecht, L. Ferreira, N. Annabi, M. A. Darabi, D. Sirabella, G. Vunjak-Novakovic, R. Langer, in *Principles of Tissue Engineering*, 5th ed. (Eds: R. Lanza, R. Langer, J. P. Vacanti, A. Atala), Academic Press, San Diego, CA **2020**, pp. 467–490.

[5] V. J. Costela-Ruiz, L. Melguizo-Rodríguez, C. Bellotti, R. Illescas-Montes, D. Stanco, C. R. Arciola, E. Lucarelli, *Int. J. Mol. Sci.* **2022**, *23*, 6356.

[6] X. Ren, M. Zhao, B. Lash, M. M. Martino, Z. Julier, *Front. Bioeng. Biotechnol.* **2019**, *7*, 469.

[7] K. W.-H. Lo, T. Jiang, K. A. Gagnon, C. Nelson, C. T. Laurencin, *Trends Biotechnol.* **2014**, *32*, 74.

[8] C. J. Gil, L. Li, B. Hwang, M. Cadena, A. S. Theus, T. A. Finamore, H. Bauser-Heaton, M. Mahmoudi, R. K. Roeder, V. Serpooshan, *J. Controlled Release* **2022**, *349*, 143.

[9] C. J. Gil, M. L. Tomov, A. S. Theus, A. Cetnar, M. Mahmoudi, V. Serpooshan, *Micromachines* **2019**, *10*, 474.

[10] C. Gil, C. Evans, L. Li, M. Vargas, G. Kabboul, T. Fulton, R. Veneziano, N. Nick, H. Bauser-Heaton, R. K. Roeder, V. Serpooshan, *Circ. Res.* **2021**, *129*, AMP207.

[11] T. A. Finamore, T. E. Curtis, J. V. Tedesco, K. Grandfield, R. K. Roeder, *Nanoscale* **2019**, *11*, 4345.

[12] L. Ning, N. Zhu, An Smith, A. Rajaram, H. Hou, S. Srinivasan, F. Mohabatpour, L. He, A. Mclnnes, V. Serpooshan, P. Papagerakis, X. Chen, *ACS Appl. Mater. Interfaces* **2021**, *13*, 25611.

[13] S. H. Kim, J. S. Kwon, J. G. Cho, K. G. Park, T. H. Lim, M. S. Kim, H. S. Choi, C. H. Park, S. J. Lee, *Bioeng. Transl. Med.* **2021**, *6*, e10216.

[14] S. Y. Nam, L. M. Ricles, L. J. Suggs, S. Y. Emelianov, *Tissue Eng., Part B: Rev.* **2015**, *21*, 88.

[15] D. V. Shepherd, J. H. Shepherd, S. M. Best, R. E. Cameron, *J. Mater. Sci. Mater. Med.* **2018**, *29*, 86.

[16] N. Trainor, Z. Cui, J. Triffitt, U. K. Tirlapur, *Tissue Eng.* **2007**, *13*, 1377.

[17] V. Farzam Rad, M. Panahi, R. Jamali, A. Darudi, A.-R. Moradi, *Biomed. Opt. Express* **2020**, *11*, 6324.

[18] M. Mahmoudi, M. Zhao, Y. Matsuura, S. Laurent, P. C. Yang, D. Bernstein, P. Ruiz-Lozano, V. Serpooshan, *Bioimpacts* **2016**, *6*, 111.

[19] A. S. Theus, L. Ning, G. Kabboul, B. Hwang, M. L. Tomov, C. N. LaRock, H. D. Bauser-Heaton, M. Mahmoudi, V. Serpooshan, *iScience* **2022**, *25*, 104947.

[20] A. A. Appel, M. A. Anastasio, J. C. Larson, E. M. Brey, *Biomaterials* **2013**, *34*, 6615.

[21] D. H. R. Kempen, M. J. Yaszemski, A. Heijink, T. E. Hefferan, L. B. Creemers, J. Britson, A. Maran, K. L. Classic, W. J. A. Dhert, L. Lu, *J. Controlled Release* **2009**, *134*, 169.

[22] S. Y. Nam, L. M. Ricles, L. J. Suggs, S. Y. Emelianov, *PLoS One* **2012**, *7*, e37267.

[23] I. F. Cengiz, J. M. Oliveira, R. L. Reis, *Biomater. Res.* **2018**, *22*, 26.

[24] S. M. Forton, M. T. Latourette, M. Parys, M. Kiupel, D. Shahriari, J. S. Sakamoto, E. M. Shapiro, *ACS Biomater. Sci. Eng.* **2016**, *2*, 508.

[25] G. Vanlenthe, H. Hagenmuller, M. Bohner, S. Hollister, L. Meinel, R. Muller, *Biomaterials* **2007**, *28*, 2479.

[26] L. E. Cole, R. D. Ross, J. M. Tilley, T. Vargo-Gogola, R. K. Roeder, *Nanomedicine* **2015**, *10*, 321.

[27] J. C. De La Vega, P. L. Esquinas, J. K. Gill, S. Jessa, B. Gill, Y. Thakur, K. Saatchi, U. O. Häfeli, *Contrast Media Mol. Imaging* **2021**, *2021*, 1250360.

[28] S. Sharifi, A. A. Saei, H. Gharibi, N. N. Mahmoud, S. Harkins, N. Dararatana, E. M. Lisabeth, V. Serpooshan, Á. Végvári, A. Moore, M. Mahmoudi, *ACS Appl Bio Mater* **2022**, *5*, 2643.

[29] M. J. Willemink, M. Persson, A. Pourmorteza, N. J. Pelc, D. Fleischmann, *Radiology* **2018**, *289*, 293.

[30] A. M. Alessio, L. R. Macdonald, *Med. Phys.* **2013**, *40*, 031108.

[31] D. P. Cormode, S. Si-Mohamed, D. Bar-Ness, M. Sigovan, P. C. Naha, J. Balegamire, F. Lavenne, P. Coulon, E. Roessl, M. Bartels, M. Rokni, I. Blevis, L. Boussel, P. Douek, *Sci. Rep.* **2017**, *7*, 4784.

[32] R. Symons, B. Krauss, P. Sahbaee, T. E. Cork, M. N. Lakshmanan, D. A. Bluemke, A. Pourmorteza, *Med. Phys.* **2017**, *44*, 5120.

[33] T. E. Curtis, R. K. Roeder, *J. Med. Imaging* **2019**, *6*, 013501.

[34] A. Pourmorteza, *Radiology* **2021**, *298*, 153.

[35] R. Roeder, T. E. Curtis, P. D. Nallathamby, L. E. Irimata, T. L. McGinnity, L. E. Cole, T. Vargo-Gogola, K. D. Cowden Dahl, *SPIE Med. Imaging* **2017**, *2017*, 10132.

[36] G. Gao, X. Cui, *Biotechnol. Lett.* **2016**, *38*, 203.

[37] C. Mandrycky, Z. Wang, K. Kim, D.-H. Kim, *Biotechnol. Adv.* **2016**, *34*, 422.

[38] A. S. Theus, L. Ning, L. Jin, R. K. Roeder, J. Zhang, V. Serpooshan, *Essays Biochem.* **2021**, *65*, 429.

[39] S. V. Murphy, A. Atala, *Nat. Biotechnol.* **2014**, *32*, 773.

[40] S. Agarwal, S. Saha, V. K. Balla, A. Pal, A. Barui, S. Bodhak, *Front. Mech. Eng.* **2020**, *6*.

[41] V. Serpooshan, M. Guvendiren, *Micromachines* **2020**, *11*, 366.

[42] C. D. Roche, C. Gentile, *J. Vis. Exp.* **2020**.

[43] A. Cetnar, M. L. Tomov, A. S. Theus, B. Lima, A. Vaidya, V. Serpooshan, in *3D Bioprinting in Medicine: Technologies, Bioinks, and Applications* (Ed: M. Guvendiren), Springer, Cham **2019**, pp. 149–162.

[44] J. B. Hu, D. A. Hu, J. W. Buikema, O. Chirikian, S. Venkatraman, V. Serpooshan, S. M. Wu, *Tissue Eng., Part A* **2017**, *23*, S158.

[45] P. Pitacco, J. M. Sadowska, F. J. O'brien, D. J. Kelly, *Acta Biomater.* **2023**, *156*, 61.

[46] M. Shokouhimehr, A. S. Theus, A. Kamalakar, L. Ning, C. Cao, M. L. Tomov, J. M. Kaiser, S. Goudy, N. J. Willett, H. W. Jang, C. N. Larock, P. Hanna, A. Lechtig, M. Yousef, J. D. S. Martins, A. Nazarian, M. B. Harris, M. Mahmoudi, V. Serpooshan, *Polymers* **2021**, *13*, 1099.

[47] X. Liu, M. Hao, Z. Chen, T. Zhang, J. Huang, J. Dai, Z. Zhang, *Biomaterials* **2021**, *272*, 120771.

[48] M. Cadena, L. Ning, A. King, B. Hwang, L. Jin, V. Serpooshan, S. A. Sloan, *Adv. Healthcare Mater.* **2021**, e2001600.

[49] N. Cubo, M. Garcia, J. F. Del Cañizo, D. Velasco, J. L. Jorcano, *Biofabrication* **2016**, *9*, 015006.

[50] M. Albanna, K. W. Binder, S. V. Murphy, J. Kim, S. A. Qasem, W. Zhao, J. Tan, I. B. El-Amin, D. D. Dice, J. Marco, J. Green, T. Xu, A. Skardal, J. H. Holmes, J. D. Jackson, A. Atala, J. J. Yoo, *Sci. Rep.* **2019**, *9*, 1856.

[51] J. Vanderburgh, J. A. Sterling, S. A. Guelcher, *Ann. Biomed. Eng.* **2017**, *45*, 164.

[52] S.-Y. Chang, T. Ching, M. Hashimoto, *Mater. Today Proc.* **2022**, *70*, 179.

[53] L. Li, C. J. Gil, T. A. Finamore, C. J. Evans, M. L. Tomov, L. Ning, A. Theus, G. Kabboul, V. Serpooshan, R. K. Roeder, *Adv. Nanobiomed. Res.* **2022**, *2*, 2200022.

[54] P. K. Jain, K. S. Lee, I. H. El-Sayed, M. A. El-Sayed, *J. Phys. Chem. B* **2006**, *110*, 7238.

[55] L. Ning, J. Shim, M. L. Tomov, R. Liu, R. Mehta, A. Mingee, B. Hwang, L. Jin, A. Mantalaris, C. Xu, M. Mahmoudi, K. C. Goldsmith, V. Serpooshan, *Adv. Sci.* **2022**, *9*, e2200244.

[56] L. Ning, R. Mehta, C. Cao, A. Theus, M. Tomov, N. Zhu, E. R. Weeks, H. Bauser-Heaton, V. Serpooshan, *ACS Appl. Mater. Interfaces* **2020**, *12*, 44563.

[57] X. Ma, M. Figl, E. Unger, M. Buschmann, P. Homolka, *Nucleic Acids Res.* **2022**, *12*, 14580.

[58] M. Gentile, *Nucleic Acids Res.* **2003**, *31*, 4779.

[59] M. L. Tomov, L. Perez, L. Ning, H. Chen, B. Jing, A. Mingee, S. Ibrahim, A. S. Theus, G. Kabboul, K. Do, S. R. Bhamidipati, J. Fischbach, K. Mccoy, B. A. Zambrano, J. Zhang, R. Avazmohammadi, A. Mantalaris, B. D. Lindsey, D. Frakes, L. P. Dasi, V. Serpooshan, H. Bauser-Heaton, *Adv. Healthcare Mater.* **2022**, *11*, e2201227.

[60] A. Schwab, R. Levato, M. D'este, S. Piluso, J. Eglin, J. Malda, *Chem. Rev.* **2020**, *120*, 11028.

[61] A. S. Theus, L. Ning, B. Hwang, C. Gil, S. Chen, A. Wombwell, R. Mehta, V. Serpooshan, *Polymers* **2020**, *12*, 2262.

[62] Z. Zhang, Y. Jin, J. Yin, C. Xu, R. Xiong, K. Christensen, B. R. Ringeisen, D. B. Chrisey, Y. Huang, *Appl. Phys. Rev.* **2018**, *5*, 041304.

[63] Yong-Ze, L. Zheng, H. Chen, W. Chen, Q. Hu, *Adv. Manuf.* **2014**, *2*, 231.

[64] J. Corona-Gomez, X. Chen, Q. Yang, *J. Funct. Biomater.* **2016**, *7*, 18.

[65] D. Chimene, R. Kaunas, A. K. Gaharwar, *Adv. Mater.* **2020**, *32*, 1902026.

[66] K. Loukelis, Z. A. Helal, A. G. Mikos, M. Chatzinikolaidou, *Gels* **2023**, *9*, 103.

[67] X. Kong, L. Wang, G. Li, X. Qu, J. Niu, T. Tang, K. Dai, G. Yuan, Y. Hao, *Mater. Sci. Eng., C* **2018**, *86*, 42.

[68] F. Xiao, J. Shi, X. Zhang, M. Hu, K. Chen, C. Shen, X. Chen, Y. Guo, Y. Li, *Front. Bioeng. Biotechnol.* **2023**, *11*, 1071692.

[69] P. Wang, L. Hao, Z. Wang, Y. Wang, M. Guo, P. Zhang, *ACS Appl. Mater. Interfaces* **2020**, *12*, 49464.

[70] S. K. Kesavan, D. Selvaraj, S. Perumal, A. Arunachalakasi, N. Ganesan, S. K. Chinnaiyan, M. Balaraman, *J. Drug Delivery Sci. Technol.* **2022**, *70*, 103247.

[71] G. López-Pérez, R. Prado-Gotor, J. A. Fuentes-Rojas, M. J. Martin-Valero, *J. Mol. Liq.* **2020**, *302*, 112381.

[72] A. Hasan, M. Morshed, A. Memic, S. Hassan, T. Webster, H. Marei, *Int. J. Nanomed.* **2018**, *13*, 5637.

[73] M. Yadid, R. Feiner, T. Dvir, *Nano Lett.* **2019**, *19*, 2198.

[74] Y. Wang, X. Wu, W. Yang, Y. Zhai, B. Xie, M. Yang, *Nanoscale Res. Lett.* **2011**, *6*, 114.

[75] C. Dannert, B. T. Stokke, R. S. Dias, *Polymers* **2019**, *11*, 275.

[76] P. Chansoria, S. Asif, K. Polkoff, J. Chung, J. A. Piedrahita, R. A. Shirwaiker, *ACS Biomater. Sci. Eng.* **2021**, *7*, 5175.

[77] S. I. Lee, F. S. Chew, *AJR Am. J. Roentgenol.* **2009**, *193*, S70.

[78] S. Shahidi, M. Janmaleki, S. Riaz, A. Sanati Nezhad, N. Syed, *Mater. Sci. Eng., C* **2021**, *126*, 112131.

[79] H. Wang, L. Zhou, J. Liao, Y. Tan, K. Ouyang, C. Ning, G. Ni, G. Tan, *J. Mater. Sci. Mater. Med.* **2014**, *25*, 2173.

[80] J. Li, D. J. Mooney, *Nat. Rev. Mater.* **2016**, *1*, 16071.

[81] K. J. Rambhia, P. X. Ma, *J. Controlled Release* **2015**, *219*, 119.

[82] X. Huang, M. A. El-Sayed, *J. Adv. Res.* **2010**, *1*, 13.

[83] Y. Yan, Y. Cao, R. Cheng, Z. Shen, Y. Zhao, Y. Zhang, G. Zhou, S. Sang, *Tissue Eng. Regen. Med.* **2022**, *19*, 59.

[84] H. Yin, M. Zhu, Y. Wang, L. Luo, Q. Ye, B. H. Lee, *Front. Soft Matter* **2023**, *2*, 1101680.

[85] M. Kus-Liskiewicz, P. Fickers, I. Ben Tahar, *Int. J. Mol. Sci.* **2021**, *22*, 10952.

[86] S. L. Mekuria, T. A. Debele, H.-C. Tsai, *ACS Appl. Mater. Interfaces* **2017**, *9*, 6782.

[87] S. M. Bittner, H. A. Pearce, K. J. Hogan, M. M. Smoak, J. L. Guo, A. J. Melchiorri, D. W. Scott, A. G. Mikos, *Tissue Eng. Part A* **2021**, *27*, 665.

[88] K. Hölzl, S. Lin, L. Tytgat, S. Van Vlierberghe, L. Gu, A. Ovsianikov, *Biofabrication* **2016**, *8*, 032002.

[89] J. W. Tashman, D. J. Shiwarski, B. Coffin, A. Ruesch, F. Lanni, J. M. Kainerstorfer, A. W. Feinberg, *Biofabrication* **2022**, *15*, 014102.

[90] V. Serpooshan, J. Zhang, *Advanced Technologies in Cardiovascular Bioengineering*, 1st ed, Springer, Cham **2022**, pp. 233–248.

[91] V. Serpooshan, M. Zhao, S. A. Metzler, K. Wei, P. B. Shah, A. Wang, M. Mahmoudi, A. V. Malkovskiy, J. Rajadas, M. J. Butte, D. Bernstein, P. Ruiz-Lozano, *Biomaterials* **2013**, *34*, 9048.

[92] D. Pretorius, V. Serpooshan, J. Zhang, *Front. Pharmacol.* **2021**, *12*, 640182.

[93] V. Serpooshan, S. Sivanesan, X. Huang, M. Mahmoudi, A. V. Malkovskiy, M. Zhao, M. Inayathullah, D. Wagh, X. J. Zhang, S. Metzler, D. Bernstein, J. C. Wu, P. Ruiz-Lozano, J. Rajadas, *Biomaterials* **2015**, *37*, 289.

[94] E. Gallo, C. Diaferia, E. Di Gregorio, G. Morelli, E. Gianolio, A. Accardo, *Pharmaceuticals* **2020**, *13*, 19.

[95] X. Hu, Y. Tang, Y. Hu, F. Lu, X. Lu, Y. Wang, J. Li, Y. Li, Y. Ji, W. Wang, D. Ye, Q. Fan, W. Huang, *Theranostics* **2019**, *9*, 4168.

[96] J. Huang, H. Bao, X. Li, Z. Zhang, *VIEW* **2022**, *3*, 20200119.

[97] Y. Zhao, D. Sultan, Y. Liu, in *Theranostic Bionanomaterials* (Ed: W. Cui, X. Zhao), Elsevier, New York **2019**, pp. 27–53.

[98] W. Poon, Y.-N. Zhang, B. Ouyang, B. R. Kingston, J. L. Y. Wu, S. Wilhelm, W. C. W. Chan, *ACS Nano* **2019**, *13*, 5785.

[99] J. Wahsner, E. M. Gale, A. Rodríguez-Rodríguez, P. Caravan, *Chem. Rev.* **2019**, *119*, 957.

[100] M. Le Fur, P. Caravan, *Metallomics* **2019**, *11*, 240.

[101] X. Tian, F. Yang, C. Yang, Y. Peng, D. Chen, J. Zhu, F. He, L. Li, X. Chen, *Int. J. Nanomed.* **2014**, *9*, 4043.

[102] J. Bahamonde, B. Brenseke, M. Y. Chan, R. D. Kent, P. J. Vikesland, M. R. Prater, *Toxicol. Pathol.* **2018**, *46*, 431.

[103] M. Longmire, P. L. Choyke, H. Kobayashi, *Nanomedicine* **2008**, *3*, 703.

[104] R. D. Ross, L. E. Cole, J. M. R. Tilley, R. K. Roeder, *Chem. Mater.* **2014**, *26*, 1187.

[105] P. M. Carvalho, M. R. Felício, N. C. Santos, S. Gonçalves, M. M. Domingues, *Front. Chem.* **2018**, *6*, 237.

[106] J. Stetefeld, S. A. Mckenna, T. R. Patel, *Biophys. Rev.* **2016**, *8*, 409.

[107] M. L. Tomov, L. Perez, L. Ning, H. Chen, B. Jing, A. Mingee, S. Ibrahim, A. S. Theus, G. Kabboul, K. Do, S. R. Bhamidipati, J. Fischbach, K. Mccoy, B. A. Zambrano, J. Zhang, R. Avazmohammadi, A. Mantalaris, B. D. Lindsey, D. Frakes, L. P. Dasi, V. Serpooshan, H. Bauser-Heaton, *Adv. Healthcare Mater.* **2021**, *10*, e2100968.

[108] A. D. Cetnar, M. L. Tomov, L. Ning, B. Jing, A. S. Theus, A. Kumar, A. N. Wijntjes, S. R. Bhamidipati, K. P. Do, A. Mantalaris, J. N. Oshinski, R. Avazmohammadi, B. D. Lindsey, H. D. Bauser-Heaton, V. Serpooshan, *Adv. Healthcare Mater.* **2021**, *10*, e2001169.

[109] M. L. Tomov, A. Cetnar, K. Do, H. Bauser-Heaton, V. Serpooshan, *J. Am. Heart Assoc.* **2019**, *8*, e014490.

[110] M. L. T. Tomov, A. Sarasani, R. Chen, H. Serpooshanw V, *Cardiovasc. Regener. Med.* **2019**, *2019*, 63.

[111] W. C. Oliver, G. M. Pharr, *J. Mater. Res.* **2004**, *19*, 3.

[112] W. C. Oliver, G. M. Pharr, *J. Mater. Res.* **1992**, *7*, 1564.

[113] V. Serpooshan, M. Julien, O. Nguyen, H. Wang, A. Li, N. Muja, J. E. Henderson, S. N. Nazhat, *Acta Biomater.* **2010**, *6*, 3978.

[114] V. Serpooshan, N. Muja, B. Marelli, S. N. Nazhat, *J. Biomed. Mater. Res. A* **2011**, *96*, 609.

[115] V. Serpooshan, Y. Liu, J. W. Buikema, F. X. Galdos, O. Chirikian, S. Paige, S. Venkatraman, A. Kumar, D. R. Rawnsley, X. Huang, D. A. Pijnappels, S. M. Wu, *Sci. Rep.* **2017**, *7*, 12590.

[116] M. D. Holbrook, D. P. Clark, C. T. Badea, *Phys. Med. Biol.* **2020**, *65*, 205012.

[117] D. P. Clark, C. T. Badea, *PLoS One* **2017**, *12*, e0180324.

[118] R. E. Alvarez, A. Macovski, *Phys. Med. Biol.* **1976**, *21*, 733.

[119] R. Ballabriga, J. Alozy, G. Blaj, M. Campbell, M. Fiederle, E. Frojdh, E. H. M. Heijne, X. Llopart, M. Pichotka, S. Procz, L. Tlustos, W. Wong, *J. Instrum.* **2013**, *8*, C02016.